HELSINKI INSTITUTE OF PHYSICS INTERNAL REPORT SERIES

HIP-2015-03

Light Propagation and Observations in Inhomogeneous Cosmological Models

Mikko Lavinto

Helsinki Institute of Physics
University of Helsinki
Finland

ACADEMIC DISSERTATION

To be presented with the permission of the Faculty of Science of the University of Helsinki for public criticism in the auditorium D101 of Physicum, Gustaf Hällströmin katu 2a, on the 27th of November 2015 at 12 o'clock.

Helsinki 2015

ISBN 978-951-51-1261-3 (printed)
ISBN 978-951-51-1262-0 (electronic)
ISSN 1455-0563
http://ethesis.helsinki.fi
Unigrafia
Helsinki 2015

Abstract

The science of cosmology relies heavily on interpreting observations in the context of a theoretical model. If the model does not capture all of the relevant physical effects, the interpretation of observations is on shaky grounds. The concordance model in cosmology is based on the homogeneous and isotropic Friedmann-Robertson-Walker metric with small perturbations. One long standing question is whether the small-scale details of the matter distribution can modify the predictions of the concordance model, or whether the concordance model can describe the universe to a high precision.

In this thesis, I discuss some potential ways in which inhomogeneities may change the interpretation of observations from the predictions of the concordance model. One possibility is that the small-scale structure affects the average expansion rate of the universe via a process called backreaction. In such a case the concordance model fails to describe the time-evolution of the universe accurately, leading to the mis-interpretation of observations. Another possibility is that the paths that light rays travel on are curved in such a way that they do not cross all regions with equal probability. If some regions are favoured and others disfavoured, the average description of the concordance model gives incorrect results.

My collaborators and I investigated the effects of voids on the CMB using second order perturbation theory and the exact Lemaître-Tolman-Bondi solution. A void has been detected in the direction of the CMB Cold Spot, but we found that contrary to the claims made in the literature, it was not large and deep enough to explain the Cold Spot. The results from perturbation theory and exact calculation agreed to a high precision, which was not surprising, as the void is fairly shallow.

We have studied a toy model of the universe, called the Swiss Cheese model, to see if the model can produce observational signals that deviate significantly from the predictions of the concordance model. We studied the backreaction in such models, and concluded that in physically motivated Swiss Cheese models, its impact on the expansion rate must be small. We also considered an unphysical model that was constructed to have the holes expand independently from the background. Even though the inhomogeneities change the expansion rate completely, the backreaction contribution to the total average expansion rate today was only at $\sim 1\%$ level.

We also studied weak lensing in a more realistic Swiss Cheese model to see how the structures change the brightness and shape of sources. We found that the simplest assumption, no change in the average flux, seemed to be violated with a probability of 98.6%. Our results agree on the magnitude of the effect, in that it should be very small, but the exact value is significantly different. There are many reasons why this may be the case, and one of the reasons is that the structures alter the area of the constant-redshift surface around the observer. However, to find conclusive proof of this, the calculation should be re-done with a higher resolution.

Acknowledgements

This thesis is based on research carried out at the Helsinki Institute of Physics and the Department of Physics at the University of Helsinki.

First, I thank my advisor Syksy Räsänen for his guidance, insight and patience. I wish to also thank the rest of my collaborators, Sebastian Szybka, Seshadri Nadathur and Shaun Hotchkiss. It has been a pleasure to work with you, and I have learned a lot from our projects.

I thank the pre-examiners of this thesis Timothy Clifton and David Mota for reading the manuscript carefully.

During my many years at the university, I have had the privilege of attending some excellent courses. The lecturers Kari Enqvist, Juha Honkonen, Hannu Koskinen, Hannu Kurki-Suonio and Claus Montonen have played a major role in kindling my interest in theoretical physics, and cosmology in particular.

I would also like to thank all of my friends and colleagues at the department. In particular I thank Samuel, Mindaugas and Toyokazu for the many hours of climbing that have certainly helped to keep me sane during my studies.

Finally, I thank my parents, the rest of my family and my partner Päivi for the constant support and encouragement during the years. Without you none of this would have been possible.

September 2015 in Helsinki
Mikko Lavinto

List of Publications

This thesis is based on the following articles [1, 2, 3].

I *Average expansion rate and light propagation in a cosmological Tardis spacetime*
M. Lavinto, S. Räsänen and S. Szybka
JCAP**12** (2013) 051

II *Can a supervoid explain the Cold Spot?*
S. Nadathur, M. Lavinto, S. Hotchkiss and S. Räsänen
Phys. Rev. **D90** (2014) no. 10 103510

III *CMB seen through random Swiss Cheese*
M. Lavinto and S. Räsänen
JCAP**10** (2015) 057

Present author's contribution

I The Swiss Cheese theorem was sketched by me and refined by S. Räsänen. I modified the code by S. Szybka and performed the calculations for the modified Swiss Cheese model, analysed the results and produced the figures. The analytic calculations were done jointly by me and S. Räsänen. The draft was written by S. Räsänen and it was jointly polished.

II The idea for the article came from the joint discussions between all of the authors. I did the calculation using the LTB profiles. The first draft was written by S. Nadathur, apart from the LTB section which was written by me. The draft was later polished by all authors.

III I modified the code by S. Szybka further to allow for a much larger simulation with a more realistic model, performed the calculations and produced the results. The first draft was written by me, which was then jointly worked on.

Contents

Chapter 1

Introduction

Today we know a great deal more about the universe than fifty years ago. Rapid development both in the theoretical and observational side of cosmology has opened a door into a domain of inquiry that used to belong only to philosophers, priests and poets – where did the universe come from, where is it going and how do we fit into it? Cosmology is a science that tries to make conclusions about the universe as a whole, often forgetting about the fine details of humans, planets, stars and even individual galaxies, focusing rather on the structure on the largest observable scales and the way galaxies cluster to form a kind of cosmic web with walls, filaments and voids.

Theory and observation are intimately linked in cosmology. The rate of the expansion of the universe is so slow compared to human length and time scales that its direct measurement would be a huge challenge. Such redshift drift experiments have been proposed already fifty years ago [4], but only now the instruments are starting to be accurate enough. Instead of direct observations, currently all cosmological information is extracted from the observations through careful modelling and data analysis, and the end result of this process is condensed into nuggets of knowledge, such as the expansion rate of space or the age of the universe. Considering how complex the universe is at the ground level, modelling the entire universe mathematically appears to be quite a challenge. It turns out however, that forgetting the messy details on the small scales makes it possible. In fact, the concordance model of cosmology is surprisingly simple. It relies on a crucial aspect of the universe called the *cosmological principle*, which states that on largest scales, the universe is homogeneous and isotropic. The cosmological principle is partly a philosophical statement, partly a theoretical prediction of inflation [5], and partly based on observation [6, 7]. However, the cosmological principle alone does not guarantee that the concordance model of cosmology is correct, as we will see.

The supernova observations of two independent groups published in 1998 [8, 9] both claimed that distant supernovae appear to be dimmer than expected for a homogeneous, spatially flat universe containing only regular matter. The simplest addition one can make to the homogeneous dust universe is adding a *cosmological constant* term [10], which allows the model universe to fit the observations well, but it comes with a price of weirdness. The model universe that fits the observations the best is currently expanding at an accelerating rate. It appears that at largest scales, gravity is not pulling matter together any more, but pushing it apart instead.

Although the cosmological constant term can exist in the equations, its value seems in many ways arbitrary and finely tuned. In particular, it seems like a strange coincidence that the cosmological constant, which does not dilute as space expands unlike regular matter, should start to influence the evolution of the universe just as cosmic large-scale structure starts forming. This *coincidence problem* has been a major motivator in re-kindling the interest in the study of inhomogeneous cosmological models, as a possible alternative explanation to the supernova observations [11, 12, 13]. It remains an open question whether the structures can have a non-

trivial effect on observation averages, and this thesis is partly attempting to contribute to the answer.

The idea that cosmic structures could affect the interpretation of observations dates back at least to the sixties, to Zel'dovich and others [14, 15, 16, 17][1]. There are two distinct possibilities for how the effect could be produced. First, the observations may inadvertently induce a systematic bias by selecting some preferred lines of sight, which do not give a fair picture of the universe as a whole. The original idea was that such biased sampling could occur if the clumps of matter were opaque, so we could only see distant objects if the light rays did not pass through any such clumps. Second, as gravity is non-linear, inhomogeneities on small scales may influence the evolution of the universe on large scales via *backreaction* [18, 19, 20, 21, 22, 23, 24].

This thesis is about the way cosmological structure formation affects the propagation of light in more complicated inhomogeneous cosmological models. The repeating theme of the thesis will be whether the standard concordance analysis gives accurate results on large scales, or if non-linear structures can produce significantly different results. The thesis is organized as follows. Chapter 2 gives a brief introduction to general relativity and some key concepts that are used throughout this thesis. Chapter 3 contains the general formalism to study propagation of light, ending in a summary of some key observations. Chapter 4 presents details of some inhomogeneous models that will be studied in more detail in Chapter 5, summarizing the research papers **I-III** [1, 2, 3]. Finally a short discussion is presented in Chapter 6.

1.1 On notation

Throughout this thesis, natural units with $c = \hbar = 1$ are used. The spacetime metric will be mostly positive, with a signature $(-,+,+,+)$. A dot stands for a derivative with respect to the coordinate time, whereas a prime will denote a derivative with respect to some other argument. A bar over a quantity indicates that it has been calculated in the homogeneous background model. The volume average over a spatial domain $\mathcal{D}$ is denoted with braces, $\langle\rangle_{\mathcal{D}}$. The average over angles in the sky is denoted with $\langle\rangle_{\Omega}$.

[1] Gunn mentions in his article [17] that the idea was also proposed by Feynman in an unpublished colloquium in 1964.

Chapter 2

Preliminaries of general relativity

2.1 Gravity

Gravity is the dominant fundamental interaction on cosmological scales. Strong and weak nuclear forces are only relevant on subatomic scales and although electromagnetism has an infinite range, electric charge is distributed so evenly throughout the universe that electromagnetic forces can be neglected. Our best understanding of gravity comes from Einstein's general theory of relativity. In it, gravity is described as geometry of the spacetime manifold that we live in. Massive objects bend the geometry of the spacetime and observers interpret this as a force because the freely falling trajectories (*geodesics*) are curved accordingly.

2.1.1 Tensors and manifolds

Vectors are objects that can be added together and multiplied by a number using the standard linear recipe. If v and u are elements of the same vector space V and a is a real number, then

$$a(v+u) = av + au \in V \ . \tag{2.1}$$

Vectors are often expressed in terms of a basis. A basis is a set of vectors e_μ that are linearly independent and span the whole vector space. Given a basis $\{e_\mu\}$, all vectors in V can be decomposed uniquely to their components

$$v = v^\mu e_\mu \equiv \sum_\mu v^\mu e_\mu \ . \tag{2.2}$$

The components of a vector are dependent on the choice of the basis, whereas the vector itself is a geometrical object and independent of its representation. We also define a dual vector space V^* that contains all linear functions from V to $\mathbb{R}$. We can define a dual basis $\{\tilde{e}^\nu\}$ and demand that it satisfies

$$\tilde{e}^\nu(e_\mu) = \delta^\nu_\mu \ . \tag{2.3}$$

Just like with vectors, any dual vector ω can be decomposed in terms of this basis

$$\omega = \omega_\mu \tilde{e}^\mu \ , \tag{2.4}$$

and so its easy to see that

$$\omega(v) = v^\mu \omega_\nu \tilde{e}^\nu(e_\mu) = v^\mu \omega_\mu \ . \tag{2.5}$$

Tensors are a generalisation of vectors and they are crucial in formulating the theory of general relativity. Vectors can be seen as tensors of rank one and real numbers as tensors of

rank zero. The components of a rank $(1,1)$ tensor T have one lower and one upper index. It can be written in terms of the basis vectors as

$$T = T_\nu{}^\mu \tilde{e}^\nu \otimes e_\mu \ , \tag{2.6}$$

where $\otimes$ denotes a tensor product. As with dual vectors, a tensor can be seen as a multilinear map from vectors and dual vectors to reals:

$$T(v,\omega) = T_\nu{}^\mu v^\nu \omega_\mu \ , \tag{2.7}$$

and this can also be consistently generalised to arbitrary tensors of rank (n,m). It is common practice to discuss tensors in terms of their components, and from now on $T_\nu{}^\mu$ will simply be called a tensor.

The spacetime of general relativity is mathematically described by a Lorentzian manifold, and it is the most fundamental concept when discussing relativity. Formally, a manifold is a topological space $(X,\mathcal{T})$ with some elementary structure[1] that is locally homeomorphic to the Euclidean space $\mathbb{R}^n$ at each point of X. The elements of X are often called *events* in general relativity. There are functions $a_i : X \longmapsto \mathbb{R}^n$ called coordinate charts. A collection of coordinate charts that covers the entire manifold is called an atlas $\mathcal{A} = \{(a_i, X_i) | i \in I\}$ where X_i is the set of events in the domain of the chart a_i.

In a differentiable manifold, at every point of the manifold there exists a vector space called tangent space T_p that contains the tangent vectors of all curves passing through the point p. A *curve* can be parametrised by a set of coordinate relations $x^\mu(s)$ and a parameter $s \in \mathbb{R}$. A convenient basis for the tangent space is the set of partial derivatives $\{\frac{\partial}{\partial x^\mu}\}$. This is called a coordinate basis. The derivative along a curve can be written using the chain rule as

$$\frac{\mathrm{d}}{\mathrm{d}s} = \frac{\mathrm{d}x^\mu}{\mathrm{d}s}\frac{\partial}{\partial x^\mu} \ . \tag{2.8}$$

The dual vector space is the space of gradients of functions, and so the dual space coordinate basis is then $\{\mathrm{d}x^\mu\}$.

The *metric tensor* $g_{\mu\nu}$ (or simply 'the metric') is a tensor that defines an inner product between the vectors living in the tangent space,

$$v \cdot u \equiv g_{\mu\nu} v^\mu u^\nu \ . \tag{2.9}$$

The metric tensor gives the length of an infinitesimal proper distance segment,

$$\mathrm{d}s^2 = g_{\mu\nu}\mathrm{d}x^\mu \mathrm{d}x^\nu, \tag{2.10}$$

and that's why it is of fundamental importance in general relativity and cosmology. The metric determinant $g = \det(g_{\mu\nu})$ is related to the infinitesimal volume element on the manifold via

$$\mathrm{d}V = \sqrt{|g|}\mathrm{d}^n x \ . \tag{2.11}$$

A Lorentzian manifold is a differentiable manifold that has a metric that has one negative eigenvalue, which corresponds to the time coordinate. The determinant of the full four-dimensional metric is negative whereas the metric determinant of any three-dimensional spatial submanifold is positive. We can also define the inverse metric $g^{\mu\nu}$ to satisfy

$$g^{\mu\nu} g_{\nu\sigma} = \delta^\mu_\sigma \ . \tag{2.12}$$

[1] $(X,\mathcal{T})$ is second countable and Hausdorff.

From the definition it follows that the metric can be used to map vectors between the tangent space and its dual, or to raise and lower vector indices

$$v^\mu = g^{\mu\nu} v_\nu; \qquad v_\mu = g_{\mu\nu} v^\nu \ . \tag{2.13}$$

A vector v^μ is called spacelike if $g_{\mu\nu} v^\mu v^\nu > 0$, timelike if $g_{\mu\nu} v^\mu v^\nu < 0$ and null if $g_{\mu\nu} v^\mu v^\nu = 0$. For a timelike curve, the proper distance $\mathrm{d}s^2$ is negative. This is weird, so in this case one often talks about the proper time $\mathrm{d}\tau = -\mathrm{d}s^2$ instead.

The final and arguably the most important piece of the structure is the *connection* $\nabla : T_p \times T_p \mapsto T_q$, which is used to move vectors between the tangent spaces of different events. The connection is a derivative operator that takes a vector y and transports it along another vector x. This is written as $\nabla_x y = z$ where z is the resulting vector. The connection coefficients $\Gamma^\alpha_{\mu\nu}$ are defined by

$$\nabla_\mu \partial_\nu = \Gamma^\alpha_{\mu\nu} \partial_\alpha \ , \tag{2.14}$$

where the shorthand notation $\nabla_\mu = \nabla_{\left(\frac{\partial}{\partial x^\mu}\right)}$ has been used. The object ∇_μ is a called the covariant derivative. Similarly to equation (2.8), a covariant derivative along a curve x^μ can be written

$$\frac{\mathrm{D}}{\mathrm{d}s} \equiv \frac{\mathrm{d}x^\mu}{\mathrm{d}s} \nabla_\mu \ . \tag{2.15}$$

A tensor is said to be parallel transported along a curve if its covariant derivative along that curve vanishes.

General relativity is a metric theory of gravity, which means that the metric is always parallel transported,

$$\nabla_\mu g_{\alpha\beta} = 0 \ . \tag{2.16}$$

The connection is also assumed to be torsion free, that is symmetric in the lower indices

$$\Gamma^\alpha_{\mu\nu} = \Gamma^\alpha_{\nu\mu} \ . \tag{2.17}$$

These conditions fix the connection completely in terms of the metric, and the result is

$$\Gamma^\alpha_{\mu\nu} = \frac{1}{2} g^{\alpha\beta} \left(\partial_\mu g_{\nu\beta} + \partial_\nu g_{\beta\mu} - \partial_\beta g_{\mu\nu} \right) \ . \tag{2.18}$$

2.1.2 Geodesics

Consider first a timelike curve $x^\mu(\lambda)$, where $\lambda \in \mathbb{R}$ is an arbitrary parameter. The curve is called a geodesic if it extremises the proper time between its endpoints A and B,

$$\tau = \int_A^B \mathrm{d}\tau = \int_A^B \sqrt{-g_{\mu\nu} \frac{\mathrm{d}x^\mu}{\mathrm{d}\lambda} \frac{\mathrm{d}x^\nu}{\mathrm{d}\lambda}} \mathrm{d}\lambda \ . \tag{2.19}$$

From the Euler-Lagrange equations, the equation that a geodesic must satisfy is

$$\frac{\mathrm{d}^2 x^\mu(\lambda)}{\mathrm{d}\lambda^2} + \Gamma^\mu_{\alpha\beta} \frac{\mathrm{d}x^\alpha(\lambda)}{\mathrm{d}\lambda} \frac{\mathrm{d}x^\beta(\lambda)}{\mathrm{d}\lambda} = \kappa(\lambda) \frac{\mathrm{d}x^\mu(\lambda)}{\mathrm{d}\lambda} \ , \tag{2.20}$$

for some function $\kappa(\lambda)$. For a timelike geodesic, we can choose the parameter λ to be the proper time along the path, which simplifies the equation as $\kappa = 0$. In fact, any *affine parameter* related to the proper time by $\lambda = a\tau + b$ has this property. For a spacelike geodesic, the same applies for the proper distance. For null geodesics, proper time and distance both vanish. Nonetheless, the geodesic equation has the same form, and a family of affine parameters λ exists. The condition that the function κ vanishes can be taken as a definition of an affine parameter in the null case.

Therefore in all cases the geodesic equation written in terms of an affine parameter λ simplifies to

$$\frac{\mathrm{d}^2 x^\mu}{\mathrm{d}\lambda^2} + \Gamma^\mu_{\alpha\beta}\frac{\mathrm{d}x^\alpha}{\mathrm{d}\lambda}\frac{\mathrm{d}x^\beta}{\mathrm{d}\lambda} = 0 \ . \tag{2.21}$$

It can be written in a shorter form in terms of the tangent vector $k^\mu = \frac{\mathrm{d}x^\mu}{\mathrm{d}\lambda}$,

$$k^\mu \nabla_\mu k^\nu = 0 \ . \tag{2.22}$$

To put it into words, the tangent vector of a geodesic is parallel transported along the geodesic.

2.1.3 Curvature

The Riemann curvature tensor can be defined in a manifold with no torsion by demanding that

$$\nabla_\alpha \nabla_\beta V^\mu - \nabla_\beta \nabla_\alpha V^\mu = R^\mu{}_{\nu\alpha\beta} V^\nu \tag{2.23}$$

holds for any vector V^μ. The left hand side can be evaluated explicitly, and this gives

$$R^\mu{}_{\nu\alpha\beta} = \partial_\alpha \Gamma^\mu_{\nu\beta} - \partial_\beta \Gamma^\mu_{\alpha\nu} + \Gamma^\mu_{\alpha\lambda}\Gamma^\lambda_{\nu\beta} - \Gamma^\mu_{\lambda\beta}\Gamma^\lambda_{\alpha\nu} \ . \tag{2.24}$$

The Riemann tensor has the following symmetries

$$R_{\mu\nu\alpha\beta} = -R_{\nu\mu\alpha\beta} = -R_{\mu\nu\beta\alpha} = R_{\alpha\beta\mu\nu} \ , \tag{2.25}$$

and

$$R_{\mu\nu\alpha\beta} + R_{\mu\alpha\beta\nu} + R_{\mu\beta\nu\alpha} = 0 \ . \tag{2.26}$$

It also satisfies the Bianchi identity,

$$\nabla_\gamma R_{\mu\nu\alpha\beta} + \nabla_\beta R_{\mu\nu\gamma\alpha} + \nabla_\alpha R_{\mu\nu\beta\gamma} = 0 \ . \tag{2.27}$$

The Ricci tensor is defined as a contraction of the 1st and 3rd indices

$$R_{\mu\nu} = R^\lambda{}_{\mu\lambda\nu} \ , \tag{2.28}$$

and the Ricci scalar is the trace of the Ricci tensor

$$R = R^\mu_{\ \mu} \ . \tag{2.29}$$

The Weyl tensor is the traceless part of the Riemann tensor that has all the same symmetries as the Riemann tensor. In n dimensions, it can be uniquely written out as

$$C_{\mu\nu\alpha\beta} = R_{\mu\nu\alpha\beta} - \frac{2}{n-2}\left(g_{\mu[\alpha}R_{\beta]\nu} - g_{\nu[\alpha}R_{\beta]\mu}\right) + \frac{2}{(n-1)(n-2)} g_{\mu[\alpha}g_{\beta]\nu}R \ . \tag{2.30}$$

The Weyl tensor is only defined for $n \geq 3$, and for $n = 3$ it vanishes identically.

2.1.4 The Einstein equation

The energy-momentum tensor $T_{\mu\nu}$ is the source of gravity in general relativity. It can be decomposed in terms of a four-velocity u^μ into

$$T_{\mu\nu} = (\rho + p)u_\mu u_\nu + p g_{\mu\nu} + q_\mu u_\nu + q_\nu u_\mu + \pi_{\mu\nu} \ , \tag{2.31}$$

where ρ the is energy density, p the is pressure, q_μ is the momentum density and $\pi_{\mu\nu}$ is the anisotropic stress of the fluid. They satisfy $q_\mu u^\mu = 0$, $\pi^\mu_\mu = 0$, $\pi_{\mu\nu} = \pi_{\nu\mu}$ and $\pi_{\mu\nu}u^\nu = 0$.

For ideal fluid, momentum density and anisotropic stress vanish, $q_\mu = 0$ and $\pi_{\mu\nu} = 0$. The energy-momentum tensor obeys a fundamental conservation law

$$\nabla_\mu T^{\mu\nu} = 0 \ . \tag{2.32}$$

The Einstein tensor is a linear, divergence-free combination of the Ricci tensor and the Ricci scalar,

$$G_{\mu\nu} = R_{\mu\nu} - \frac{1}{2} R g_{\mu\nu}; \qquad \nabla_\mu G^\mu{}_\nu = 0 \ , \tag{2.33}$$

and it can be used to write the Einstein field equation,

$$G_{\mu\nu} + \Lambda g_{\mu\nu} = 8\pi G T_{\mu\nu} \ , \tag{2.34}$$

where Λ is the cosmological constant. The Einstein equation is the equation of motion for the metric and the energy-momentum tensor. In short, it links together the curvature of the universe (or 'gravity') on the left-hand side, and the matter content of the universe on the right-hand side. The matter acts locally to change the Ricci tensor, whereas the non-local effects are 'stored' in the Weyl tensor. The Weyl tensor is not directly modified by the Einstein equation, but instead non-local effects are generated from the local curvature by the Bianchi identity (2.27).

2.2 The homogeneous Friedmann-Robertson-Walker solution

Our universe is extremely inhomogeneous on the scales of planets and stars and galaxies. However, if one zooms out far enough, on scales greater than $\sim$ 100Mpc the universe looks nearly homogeneous and isotropic so for the first approximation it makes sense to look for such a solution. The solution that describes a homogeneous and isotropic universe is the Friedmann-Robertson-Walker (FRW)-metric [25, 26, 27, 28, 29],

$$\mathrm{d}s^2 = -\mathrm{d}t^2 + a^2(t) \left(\frac{\mathrm{d}r^2}{1 - Kr^2} + r^2(\mathrm{d}\theta^2 + \sin^2\theta \mathrm{d}\phi^2) \right) \ , \tag{2.35}$$

where $a(t)$ is a scale factor that describes how the universe expands or contracts and K describes the curvature of the spatial hypersurfaces. Given this form of the metric metric, the Einstein equations can be solved to give two independent equations, the Friedmann equations:

$$\frac{\dot{a}^2}{a^2} = \frac{8\pi G}{3}\rho - \frac{K}{a^2} + \frac{\Lambda}{3} \tag{2.36}$$

$$\frac{\ddot{a}}{a} = -\frac{4\pi G}{3}(\rho + 3p) + \frac{\Lambda}{3} \ . \tag{2.37}$$

The dot denotes a derivative with respect to time, and ρ and p are the total energy density and pressure of the averaged fluid. The Hubble rate

$$H(t) \equiv \frac{\dot{a}}{a} \tag{2.38}$$

gives the relative expansion rate of the universe.

The energy-momentum conservation equation gives

$$\dot{\rho} + 3H(\rho + p) = 0 \ , \tag{2.39}$$

but this constraint is not independent from the Friedmann equations. Given different fluids with different equation of state parameters w, satisfying $p = w\rho$ and

$$w_m = 0, \qquad w_r = 1/3, \qquad w_\Lambda = -1 \ , \tag{2.40}$$

we can write (2.36) as

$$H^2 = H_0^2 \left[\Omega_\Lambda + \Omega_K \left(\frac{a}{a_0} \right)^{-2} + \Omega_m \left(\frac{a}{a_0} \right)^{-3} + \Omega_r \left(\frac{a}{a_0} \right)^{-4} \right] , \tag{2.41}$$

where H_0 is the Hubble rate today and Ω_m, Ω_r, Ω_K and Ω_Λ are the fractions of dust, radiation, curvature and cosmological constant of the total energy budget of the universe today, which satisfy by definition

$$\Omega_m + \Omega_r + \Omega_K + \Omega_\Lambda = 1 \ . \tag{2.42}$$

Based on recent observations [30], these have the values $\Omega_m = 0.3$, $\Omega_r \sim 10^{-5}$, $|\Omega_K| \leq 0.001$ and $\Omega_\Lambda = 0.7$. The Hubble parameter's value is $H_0 \simeq 70\text{km/s/Mpc} \equiv 100h\text{km/s/Mpc}$ with $h \simeq 0.7$.

We can use the form (2.41) to solve time as a function of the scale factor

$$t = H_0^{-1} \int \mathrm{d}a \left[\Omega_\Lambda + \Omega_K \left(\frac{a}{a_0} \right)^{-2} + \Omega_m \left(\frac{a}{a_0} \right)^{-3} + \Omega_r \left(\frac{a}{a_0} \right)^{-4} \right]^{-1/2} , \tag{2.43}$$

and after solving the integral, this expression can be inverted to find the scale factor as a function of time. Analytic solutions can be found for cases where only two components are non-zero. In the general case, the integral is an elliptic function with no analytic solutions in terms of elementary functions, and it needs to be solved numerically.

2.3 Submanifolds

The machinery for constructing and describing submanifolds is needed in several parts of this thesis. In the next section, we need to split the full four-dimensional spacetime into space and time separately by constructing a foliation of 3-dimensional spatial slices. Also light propagation in Section 3.4 and the Swiss Cheese construction in Section 4.3 require some parts of the mathematics summarised here.

2.3.1 Hypersurfaces

A hypersurface is an $(n-1)$-dimensional submanifold Σ living in an n-dimensional manifold. The submanifold can conveniently be characterised via its normal vector n^μ, which can in this context be spacelike or timelike[2], and it can be normalised to $n_\mu n^\mu = \epsilon = \pm 1$. The projection tensor

$$h_{\alpha\beta} \equiv g_{\alpha\beta} - \epsilon n_\alpha n_\beta \tag{2.44}$$

can be used to project tensors into the hypersurface. It satisfies $h_\alpha^{\ \lambda} h_\lambda^{\ \beta} = h_\alpha^{\ \beta}$ and $h_{\alpha\beta} h^{\alpha\beta} = 3$. It also defines an induced three-metric on the hypersurface. Let y^a, $a \in \{1,2,3\}$ be new coordinates on the hypersurface, defined via coordinate relations $x^\alpha = x^\alpha(y^a)$. The induced metric, or the first fundamental form on the hypersurface is then

$$h_{ab} \equiv h_{\alpha\beta} \frac{\partial x^\alpha}{\partial y^a} \frac{\partial x^\beta}{\partial y^b} = h_{\alpha\beta} e_a^\alpha e_b^\beta \ , \tag{2.45}$$

where the vectors e_a^α are tangent to curves in Σ and so $e_a^\alpha n_\alpha = 0$. The induced metric is a tensor living on the submanifold Σ, so it behaves as a scalar under the full spacetime coordinate

[2] Null hypersurfaces can also be considered, but they require slightly different kind of treatment, which is not needed in this thesis.

transformations $x^\alpha \to x^{\alpha'}$ but as a two-tensor under the hypersurface coordinate transformations $y^a \to y^{a'}$. The extrinsic curvature tensor, or the second fundamental form $K_{\alpha\beta}$ is defined

$$K_{\alpha\beta} \equiv h_\alpha{}^\mu h_\beta{}^\nu \nabla_\mu n_\mu \ . \tag{2.46}$$

Although it is not immediately obvious, the extrinsic curvature tensor is symmetric in its indices. If n^μ is the tangent of a geodesic, $K_{\alpha\beta}$ is automatically confined onto the hypersurface, but in general it must be projected. In terms of the coordinates y it is written as

$$K_{ab} = K_{\alpha\beta} e_a^\alpha e_b^\beta = e_a^\alpha e_b^\beta \nabla_\alpha n_\beta \ . \tag{2.47}$$

The hypersurface has its own connection as well,

$$\Gamma^c_{ab} = e^c_\gamma e^\beta_b \nabla_\beta e^\gamma_a \ , \tag{2.48}$$

which is compatible with the induced metric. The connection defines a covariant derivative as usual

$$\tilde{\nabla}_a A^c = \partial_a A^c + \Gamma^c_{ab} A^b \ , \tag{2.49}$$

and (2.48) and (2.49) can in turn be used to define the Riemann curvature tensor (2.23) on Σ. The three-dimensional curvature tensor is not just the projection of the full four-dimensional tensor, but instead

$$R_{\alpha\beta\gamma\delta} e_a^\alpha e_b^\beta e_c^\gamma e_d^\delta = R_{abcd} + \epsilon(K_{ad}K_{bc} - K_{ac}K_{bd}) \ . \tag{2.50}$$

Projecting one index along n^μ gives

$$R_{\mu\alpha\beta\gamma} n^\mu e_a^\alpha e_b^\beta e_c^\gamma = \tilde{\nabla}_c K_{ab} - \tilde{\nabla}_b K_{ac} \ . \tag{2.51}$$

These two equations are called the Gauss-Codazzi equations. Contracting (2.50) and (2.51) gives

$$-2G_{\alpha\beta} n^\alpha n^\beta = \epsilon\ {}^{(3)}R + (K_{ab}K^{ab} - K^2) \tag{2.52}$$

$$G_{\alpha\beta} e_a^\alpha n^\beta = \tilde{\nabla}_b K_a{}^b - \partial_a K \ , \tag{2.53}$$

where ${}^{(3)}R \equiv h^{ab} R^c{}_{acb}$ is the Ricci scalar of Σ. These can be used with the Einstein equation to produce the Hamiltonian constraint equation [31] (page 80)

$${}^{(3)}R + K^2 - K_{\alpha\beta}K^{\alpha\beta} = 16\pi G T_{\alpha\beta} n^\alpha n^\beta \ , \tag{2.54}$$

This equation is the generalisation of the first Friedmann equation (2.36). The generalisation of the second Friedmann equation is the Raychaudhuri equation, and that will be derived next.

2.3.2 Movement of massive test particles

The Einstein equation (2.34) is too complicated to solve for most cases. Some general progress can be made however, by choosing a timelike vector that defines a global time coordinate. We can then define a foliation of the spacetime into spatial hyperslices, defined at an instant of this global time coordinate.

A congruence is a set of curves that fill a small spacetime region so that one curve passes through every point without intersecting each other. Consider a congruence of timelike geodesics $x^\mu(\tau)$ with tangent vector $u^\mu = \frac{dx^\mu}{d\tau}$. We can construct another curve $x^\mu(s)$ with tangent vector $\xi^\mu = \frac{dx^\mu}{ds}$ that intersects the congruence perpendicular to it, $\xi^\mu u_\mu = 0$. Geometrically, ξ^μ is

a separation vector between two nearby geodesics, and by looking at how it evolves, we can investigate how the geodesic bundle diverges (or converges). By construction, ξ^μ satisfies

$$\frac{\mathrm{d}}{\mathrm{d}\tau}\xi^\mu = \frac{\mathrm{d}}{\mathrm{d}\tau}\frac{\mathrm{d}x^\mu}{\mathrm{d}s} = \frac{\mathrm{d}}{\mathrm{d}s}\frac{\mathrm{d}x^\mu}{\mathrm{d}\tau} = \frac{\mathrm{d}}{\mathrm{d}s}u^\mu, \tag{2.55}$$

and since the connection is torsion-free, it also satisfies

$$u^\nu\nabla_\nu\xi^\mu = \xi^\nu\nabla_\nu u^\mu \equiv B_\nu{}^\mu\xi^\nu \ , \tag{2.56}$$

where the last identity follows from the fact that u^μ is a geodesic, so the tensor $B_{\mu\nu} \equiv \nabla_\mu u_\nu$ is purely transverse to u^μ. In words, the tensor $B_{\mu\nu}$ tells how the separation vector fails to be parallel transported along u^μ.

The expansion tensor $B_{\mu\nu}$ can be decomposed into trace, symmetric traceless and antisymmetric parts,

$$B_{\mu\nu} = \nabla_\mu u_\nu = \frac{1}{3}\theta h_{\mu\nu} + \sigma_{\mu\nu} + \omega_{\mu\nu} \ , \tag{2.57}$$

where $\theta \equiv \nabla_\mu u^\mu$ is the expansion scalar[3], $\sigma_{\mu\nu} \equiv \nabla_{(\mu}u_{\nu)} - \frac{1}{3}\theta h_{\mu\nu}$ is the dust shear tensor and $\omega_{\mu\nu} \equiv \nabla_{[\mu}u_{\nu]}$ is the dust rotation tensor. The expansion scalar describes how the congruence expands (if $\theta > 0$) or shrinks (if $\theta < 0$), the shear tensor describes how the shape of the congruence is distorted and rotation tensor describes how its orientation rotates.

We can derive an equation of motion for the scalar θ by differentiating it along the geodesic u^μ,

$$\begin{aligned}
\frac{\mathrm{d}\theta}{\mathrm{d}\tau} &= u^\mu\nabla_\mu\nabla_\nu u^\nu && (2.58)\\
&= u^\mu\left(\nabla_\nu\nabla_\mu u^\nu + R^\nu{}_{\rho\mu\nu}u^\rho\right) && (2.59)\\
&= \nabla_\nu(u^\mu\nabla_\mu u^\nu) - (\nabla_\nu u^\mu)(\nabla_\mu u^\nu) - R_{\mu\nu}u^\mu u^\nu && (2.60)\\
&= -B_\nu{}^\mu B_\mu{}^\nu - R_{\mu\nu}u^\mu u^\nu && (2.61)\\
&= -\frac{1}{3}\theta^2 - \sigma_{\mu\nu}\sigma^{\mu\nu} + \omega_{\mu\nu}\omega^{\mu\nu} - R_{\mu\nu}u^\mu u^\nu && (2.62)\\
&\equiv -\frac{1}{3}\theta^2 - 2\sigma^2 + 2\omega^2 - R_{\mu\nu}u^\mu u^\nu \ , && (2.63)
\end{aligned}$$

where the Riemann tensor definition (2.23) is used on the second row and the geodesic equation on the fourth. Equation (2.63) is the *Raychaudhuri equation* [32]. Similar equations can be derived for the shear and vorticity tensors [33, 34], but they are not needed in this thesis.

Both $\sigma_{\mu\nu}\sigma^{\mu\nu} \equiv 2\sigma^2$ and $\omega_{\mu\nu}\omega^{\mu\nu} \equiv 2\omega^2$ are positive-definite, but the vorticity term enters equation (2.63) with a reversed sign due to its antisymmetry. If the vector field u^μ is rotationless, $\omega_{\mu\nu} = 0$ and the curvature term is positive, $R_{\mu\nu}u^\mu u^\nu > 0$[4], then we see that $\frac{\mathrm{d}\theta}{\mathrm{d}\tau}$ is always negative. The expansion rate decreases along the geodesic, so converging geodesics converge faster and diverging geodesics diverge slower until they begin to converge. In other words, gravity is an attractive force. Both of the conditions assumed above are non-trivial though. Galaxies rotate, and this rotation counteracts gravity's pull. In such a system, the rotation term in (2.63) cancels with the other terms, making the system stationary. In the real universe there is also observational indication that $R_{\mu\nu}u^\mu u^\nu$ is in fact negative. For an ideal fluid, using (2.31) and (2.34), it can be written as

$$R_{\mu\nu}u^\mu u^\nu = 4\pi G(\rho + 3p) - \Lambda \ . \tag{2.64}$$

On the largest scales, the expansion of the universe appears to be accelerating, which has lead people to conclude that the cosmological constant term must be dominating on the largest scales.

[3] Note that throughout this thesis, θ is used both for the angular coordinate and the expansion rate. It should be clear from the context which θ is meant.

[4] This is called the weak energy condition, see e.g. [35]

2.4 Averaged quantities and backreaction

Consider a scalar quantity f defined on the spatial hypersurface. The spatial average is taken by integrating over a spatial domain $\mathcal{D}$ with induced metric h_{ab}, volume element $\mathrm{d}V = \sqrt{\det h}\ \mathrm{d}^3x$ and volume $V_\mathcal{D}$,

$$\langle f \rangle_\mathcal{D} \equiv V_\mathcal{D}^{-1} \int_\mathcal{D} \mathrm{d}V f \ . \tag{2.65}$$

As the volume depends on time, the time derivatives and averages do not commute, but instead they satisfy the relation

$$\frac{\partial}{\partial t}\langle f \rangle_\mathcal{D} = \langle \dot{f} \rangle_\mathcal{D} - \langle \theta \rangle_\mathcal{D} \langle f \rangle_\mathcal{D} + \langle \theta f \rangle_\mathcal{D} \ . \tag{2.66}$$

An average scale factor can be defined in the domain $\mathcal{D}$,

$$a_\mathcal{D} \equiv \left(\frac{\dot{V}_\mathcal{D}}{V_\mathcal{D}} \right)^{1/3} \ . \tag{2.67}$$

There are two other local scalar equations that can be written [33, 36] in addition to the Raychaudhuri equation. Assuming further that pressure and vorticity are negligibly small, we have

$$\dot{\theta} + \frac{1}{3}\theta^2 = -2\sigma^2 - 4\pi G\rho + \Lambda \tag{2.68}$$

$$\frac{1}{3}\theta^2 = 8\pi G\rho - \frac{1}{2}{}^{(3)}R + \Lambda + \sigma^2 \tag{2.69}$$

$$\dot{\rho} + \theta\rho = 0 \ . \tag{2.70}$$

The first equation is the Raychaudhuri equation, the second equation is the Hamiltonian constraint (2.54) using (2.57) and the third equation arises from energy-momentum conservation (2.32). Taking volume average on both sides of the equations gives the evolution equations for the average scale factor

$$\frac{\ddot{a}_\mathcal{D}}{a_\mathcal{D}} = -\frac{4\pi G}{3}\langle \rho \rangle_\mathcal{D} + \frac{1}{3}\Lambda + \frac{1}{3}\mathcal{Q}_\mathcal{D} \tag{2.71}$$

$$\frac{\dot{a}_\mathcal{D}^2}{a_\mathcal{D}^2} = \frac{8\pi G}{3}\langle \rho \rangle_\mathcal{D} + \frac{1}{3}\Lambda - \frac{1}{6}{}^{(3)}R - \frac{1}{6}\mathcal{Q}_\mathcal{D} \tag{2.72}$$

$$\frac{\partial}{\partial t}\langle \rho \rangle_\mathcal{D} + 3\frac{\dot{a}_\mathcal{D}}{a_\mathcal{D}}\langle \rho \rangle_\mathcal{D} = 0 \ , \tag{2.73}$$

with the backreaction variable $\mathcal{Q}_\mathcal{D}$ defined as

$$\mathcal{Q}_\mathcal{D} \equiv \frac{2}{3}\left\langle \theta^2 - \langle \theta \rangle_\mathcal{D}^2 \right\rangle_\mathcal{D} - 2\langle \sigma^2 \rangle_\mathcal{D} \ . \tag{2.74}$$

These equations are known as the Buchert equations [23, 24]. Comparing to the Friedmann equations (2.36), averaging has generated a new backreaction term proportional to $\mathcal{Q}_\mathcal{D}$, which affects the time-evolution of the average scale factor. The size of the backreaction term should be compared to the average expansion rate squared.

Generating a large backreaction term has proved to be difficult though. Some examples of inhomogeneous models with a large backreaction component exist in the literature [37, 38], but these are models with huge, horizon-sized inhomogeneities. The problem in constructing more realistic models is that the shear term tends to conspire with the variance term to cancel so that the backreaction term is small even when variation in the expansion rate is large. The cancellation is exact in the Newtonian case [23], in which the backreaction term is a boundary

term. It also vanishes in first order perturbation theory [39]. It might be tempting to consider a model with disjoint FRW regions as a proof of concept for backreaction [40, 41, 42]: Suppose for simplicity that there are two separate regions of FRW spacetime with expansion rates H_0 and $-H_0$ and with equal volumes at time t_0. The average of the expansion rate is zero, but $\langle\theta^2\rangle_{\mathcal{D}} = H_0^2$, so the backreaction term seems to be of same size as the actual expansion rate. However, there is a problem. The universe is not made out of disjoint regions. In a realistic scenario, these regions would be connected smoothly, and in these connection regions, shear is large, leading again to some degree of cancellation between the two terms [43]. It is still under dispute whether there are realistic situations where backreaction can give a significant contribution to the time evolution of the real universe [44, 45, 46], or whether it will necessarily be small [47, 48, 49, 50].

Chapter 3

Light propagation

The formalism that is presented in this chapter describes all electromagnetic radiation (radio waves, microwaves, x-rays and so forth) and so the word light is used as a shorthand. Nearly all observations in cosmology are made via light, so knowing how light propagates through the universe is critical in being able to interpret observations consistently and to extract information about the universe. To calculate distances to faraway objects, we need to understand how the geodesics that form the object's image behave as they travel through the universe. The next sections go through the basics of the propagation of light in inhomogeneous spacetimes using the Sachs formalism, which describes the evolution of a congruence of null geodesics. At the end of the chapter there is a brief overview of some cosmological observations that will be referenced in later chapters.

3.1 Geometrical optics approximation

The propagation of electromagnetic radiation is classically described by the Maxwell's equations. In Minkowski spacetime, solving Maxwell's equations is straightforward [51], but in curved spacetimes analytic solutions can be found only in the simplest cases. Furthermore, plane waves are in general not a solution. Luckily most cosmological applications are in a setting where the solution can be approximated as a plane wave. This is true if the spacetime curvature is nearly constant on the length scales of the light beam width and time scales of the photon's frequency. This is called the *geometrical optics approximation* [52] (page 93), and in this chapter and onwards, it is always assumed to hold. The most important consequence of the geometrical optics approximation is that light travels on null geodesics.

3.2 Redshift

'A photon's redshift is the relative change in its frequency as it travels from the observer to the source,

$$z \equiv \frac{\omega_S - \omega_O}{\omega_O} \ . \tag{3.1}$$

The frequency is the time component of the photon wave vector $k^\mu = \frac{dx^\mu}{d\lambda}$, so we can write

$$1 + z = \frac{u^S_\mu k^\mu_S}{u^O_\mu k^\mu_O} \ , \tag{3.2}$$

where u^S and u^O are the four-velocities of the source and the observer. If we take both the observer and the source to be at rest with respect to a dust ideal fluid with four-velocity u^μ, it

is useful to decompose the wave vector into

$$k^\mu = \omega(u^\mu + e^\mu) \ , \tag{3.3}$$

with components parallel and perpendicular to the matter flow, $u_\mu e^\mu = 0$ and $e_\mu e^\mu = 1$, so $\omega = -u_\mu k^\mu$ is the photon energy measured by observer with four-velocity u^μ.

The redshift can be solved by writing a differential equation for the wave vector time component,

$$\frac{\mathrm{d}\omega}{\mathrm{d}\lambda} = k^\mu \nabla_\mu \omega = -\omega^2 \left(\frac{1}{3}\theta + \sigma_{\mu\nu} e^\mu e^\nu \right) \ , \tag{3.4}$$

and this can be used to write redshift as an integral

$$1 + z = \exp\left[\int_{t_E}^{t_O} \mathrm{d}t \left(\frac{1}{3}\theta + \sigma_{\mu\nu} e^\mu e^\nu \right) \right] \ , \tag{3.5}$$

where t_E and t_O are the times of emission and observation, respectively.

In the homogeneous and isotropic FRW case, the redshift simplifies greatly as $\theta = 3H = 3\frac{\dot{a}}{a}$ and $\sigma_{\mu\nu} = 0$. Therefore

$$1 + \bar{z} = \exp\left[\int_{t_E}^{t_O} \mathrm{d}t \left(\frac{\dot{a}}{a} \right) \right] = \exp\left[\int_{a_S}^{a_O} \frac{\mathrm{d}a}{a} \right] = \frac{a_O}{a_S} \ , \tag{3.6}$$

where the bar is used to denote an observable calculated in a background FRW universe.

Redshift can be used as an indicator of distance in an expanding universe. Expansion increases the redshift, and objects further away have usually more expansion of space between them and us. However, this is not always true, and redshift is also affected by shearing of the space.

3.3 Distances

The light cone of an observer is the collection of geodesics that converge at the observer's location. In cosmology, distances along the light cone are more interesting, as they can be easily related to observations (which are made using light). There are two distances in particular that are often used. The luminosity distance D_L is defined in terms of the measured photon flux F and the intrinsic luminosity L,

$$D_L \equiv \sqrt{\frac{L}{4\pi F}} \ . \tag{3.7}$$

The fainter an object with some intrinsic luminosity looks, the further away it is. The angular diameter distance D_A is defined in terms of the source's physical size s and the angle it subtends on the sky θ,

$$D_A \equiv \frac{s}{\theta} \ . \tag{3.8}$$

The smaller an object with some fixed size looks on the sky, the further away it is.

In the FRW case, a formula for the angular diameter distance can be written in an analytic form. From the FRW metric (2.35), the viewing angle θ and proper size s are related via $\mathrm{d}s = a(t) r \mathrm{d}\theta$, so $\bar{D}_A = a(t) r$. It is straightforward to solve for r along a null radial geodesic, $\mathrm{d}s^2 = 0$, which gives depending on the sign of the curvature constant K [53],

$$\bar{D}_A = a(t) \begin{cases} K^{-1/2} \sin\left(\sqrt{K}\chi \right), & \text{for } K > 0 \\ \chi, & \text{for } K = 0 \\ (-K)^{-1/2} \sinh\left(\sqrt{-K}\chi \right), & \text{for } K < 0 \end{cases} \tag{3.9}$$

with

$$\chi \equiv \int \frac{\mathrm{d}a'}{a'^2 H(a')} \ . \tag{3.10}$$

A more geometrical definition is useful for calculating these distances in the general case [33, 52]. Consider a thin beam of light with cross-sectional area $\mathrm{d}A$ that originates from the observer at a solid angle $\mathrm{d}\Omega_O$, meaning that the area at observer's location vanishes, $\mathrm{d}A_O = 0$. Then the angular diameter distance[1] to a source S is

$$D_A = \sqrt{\frac{\mathrm{d}A_S}{\mathrm{d}\Omega_O}} \ . \tag{3.11}$$

Interchanging the observer and source so that the beam originates from the source at a solid angle $\mathrm{d}\Omega_S$ and arrives at the observer with an area $\mathrm{d}A_O$ gives the *corrected luminosity distance*

$$\hat{D}_L = \sqrt{\frac{\mathrm{d}A_O}{\mathrm{d}\Omega_S}} \ , \tag{3.12}$$

related to the luminosity distance via $D_L = (1+z)\hat{D}_L$ where the extra factor of the source redshift $1+z$ arises from the photon redshift factor. It turns out that the angular diameter distance and the luminosity distance are related to one another via the Etherington reciprocity theorem [54, 55],

$$D_L = (1+z)^2 D_A \ , \tag{3.13}$$

making them practically interchangeable.

3.4 Null geodesic congruences

Just as in section 2.3, we can construct a formalism for describing congruences of null geodesics. Consider a central geodesic $x^\mu(\lambda)$ with a null tangent vector k^μ and define an auxiliary tensor

$$B_{\mu\nu} \equiv \nabla_\mu k_\nu \ , \tag{3.14}$$

which is symmetric in its indices and satisfies $B_{\mu\nu}k^\mu = 0$. Then define a separation vector between two nearby geodesics by $\xi^\mu = \frac{\mathrm{d}x^\mu}{\mathrm{d}s}$, which itself is a tangent vector to another geodesic, and which is perpendicular to k everywhere, $k_\mu \xi^\mu = 0$. It is easily seen that this vector evolves along the geodesic as

$$\frac{\mathrm{D}}{\mathrm{d}\lambda}\xi^\nu = B_\mu{}^\nu \xi^\mu \ , \tag{3.15}$$

just as in (2.56). We are looking to calculate properties of ξ^μ perpendicular to k^μ, but since k^μ is null, requiring $\xi^\mu k_\mu = 0$ still allows for ξ^μ to have a component parallel to k^μ.

It turns out that the submanifold transverse to a null vector k^μ is two-dimensional and it will not be uniquely defined, unlike in Section 2.3. To construct the submanifold, we need to define an auxiliary vector field l^μ, which also is perpendicular to the surface. Without loss of generality we can choose it to be normalized as $k_\mu l^\mu = -1$. Then the projection tensor

$$\tilde{h}_{\mu\nu} \equiv g_{\mu\nu} + k_\mu l_\nu + l_\mu k_\nu \tag{3.16}$$

can be used to find the piece of ξ^μ that is projected onto the surface and therefore also transverse to k^μ,

$$\tilde{\xi}^\mu = \tilde{h}_\nu{}^\mu \xi^\nu = \xi^\mu + k^\mu l_\nu \xi^\nu \ . \tag{3.17}$$

[1] To be precise, this should be called 'area distance' as it depends on the area instead of diameter and solid angle instead of angle, but these terms can be used interchangeably in nearly all cases.

Tilde is used to denote quantities that are projected onto the surface. The transverse vector satisfies

$$k^\alpha \nabla_\alpha \tilde{\xi}^\beta = \tilde{h}_\gamma{}^\beta k^\alpha \nabla_\alpha \xi^\gamma + \xi^\gamma k^\alpha \nabla_\alpha \tilde{h}_\gamma{}^\beta = \tilde{h}_\gamma{}^\beta B_\alpha{}^\gamma \xi^\alpha + (\nabla_\alpha l_\gamma)\xi^\gamma k^\alpha k^\beta \ , \tag{3.18}$$

and projecting the resulting vector gives

$$\begin{aligned}
(k^\alpha \nabla_\alpha \tilde{\xi}^\beta)\tilde{} &= \tilde{h}_\gamma{}^\beta k^\alpha \nabla_\alpha \left(\xi^\gamma + k^\gamma l_\nu \xi^\nu\right) && (3.19)\\
&= \tilde{h}_\gamma{}^\beta B_\alpha{}^\gamma \xi^\alpha && (3.20)\\
&= \tilde{h}_\gamma{}^\beta \tilde{h}_\delta{}^\alpha B_\alpha{}^\gamma \tilde{\xi}^\delta && (3.21)\\
&= \tilde{B}_\alpha{}^\beta \tilde{\xi}^\alpha \ . && (3.22)
\end{aligned}$$

This equation describes the separation of geodesics in the surface perpendicular to k^μ, so it is the null counterpart of (2.56).

As in the three-dimensional case (2.57), the projected tensor $\tilde{B}_{\alpha\beta}$ can be decomposed into a trace and a traceless symmetric and antisymmetric tensor parts,

$$\tilde{B}_{\alpha\beta} \equiv \tilde{h}_\alpha{}^\mu \tilde{h}_\beta{}^\nu B_{\mu\nu} = \frac{1}{2}\tilde{\theta}\tilde{h}_{\alpha\beta} + \tilde{\sigma}_{\alpha\beta} + \tilde{\omega}_{\alpha\beta} \ , \tag{3.23}$$

with

$$\begin{aligned}
\tilde{\theta} &= \tilde{h}_\alpha{}^\beta \nabla_\beta k^\alpha = \nabla_\alpha k^\alpha && (3.24)\\
\tilde{\sigma}_{\alpha\beta} &= \tilde{B}_{(\alpha\beta)} - \frac{1}{2}\tilde{\theta}\tilde{h}_{\alpha\beta} && (3.25)\\
\tilde{\omega}_{\alpha\beta} &= \tilde{B}_{[\alpha\beta]} = 0 \ . && (3.26)
\end{aligned}$$

The trace part $\tilde{\theta}$ is independent of the choice of l^μ, and it describes the expansion and convergence of the projected beam[2]. The traceless symmetric part $\tilde{\sigma}_{\alpha\beta}$ describes the shearing of the beams projection and the traceless antisymmetric part $\tilde{\omega}_{\alpha\beta}$ describes its rotation. The antisymmetric part is however identically zero in the geometrical optics approximation due to Frobenius' theorem [56, 31, 57].

At this point it is convenient to proceed to define a set of basis vectors on the two dimensional surface, s^α_A where $A \in \{1, 2\}$ is an index that labels the directions on the surface. The basis vectors should be orthonormal and parallel transported along the curve,

$$s^\alpha_A s^\beta_B g_{\alpha\beta} = \delta_{AB} \ , \quad k^\beta \nabla_\beta s^\alpha_A = 0 \ . \tag{3.27}$$

Note that this is not a coordinate basis, but instead a vielbein[3] basis [34]. Since the surface is orthogonal to k^α and l^α,

$$k_\alpha s^\alpha_A = 0 \ , \quad l_\alpha s^\alpha_A = 0 \ . \tag{3.28}$$

The projected expansion tensor can be written in terms of s^α_A as

$$\tilde{B}_{AB} = s^\alpha_A s^\beta_B \tilde{B}_{\alpha\beta} = \frac{1}{2}\tilde{\theta}\delta_{AB} + \tilde{\sigma}_{AB} \ . \tag{3.29}$$

The basis $(k^\mu, l^\mu, s^\mu_1, s^\mu_2)$ is called the Sachs basis.

The traceless symmetric part of $\tilde{B}_{AB}$ can be written in terms of two real numbers (or alternatively in terms of one complex number)

$$\tilde{\sigma}^A{}_B = \begin{pmatrix} \tilde{\sigma}_1 & \tilde{\sigma}_2 \\ \tilde{\sigma}_2 & -\tilde{\sigma}_1 \end{pmatrix} = \tilde{\sigma} \begin{pmatrix} \cos\chi & \sin\chi \\ \sin\chi & -\cos\chi \end{pmatrix} \ , \tag{3.30}$$

[2] Note that sometimes $\tilde{\theta}$ is defined with an additional factor of $\frac{1}{2}$

[3] In four dimensions, it's often called vierbein, or tetrad

where χ is the angle between the basis vectors s^α_A and the principal axes of shearing and $\tilde{\sigma} \equiv \sqrt{\tilde{\sigma}_1^2 + \tilde{\sigma}_2^2}$. In the directions of the principal axes, the beam is stretched and squeezed by amounts $\frac{1}{2}\tilde{\theta} + \tilde{\sigma}$ and $\frac{1}{2}\tilde{\theta} - \tilde{\sigma}$. From this it is easy to verify that

$$\tilde{\sigma}^2 \equiv \frac{1}{2}\tilde{\sigma}_{\alpha\beta}\tilde{\sigma}^{\alpha\beta} = \frac{1}{2}\tilde{\sigma}_{AB}\tilde{\sigma}^{AB} \ , \tag{3.31}$$

$$\tilde{\sigma}^A{}_C\tilde{\sigma}^C{}_B = \begin{pmatrix} \tilde{\sigma}_1 & \tilde{\sigma}_2 \\ \tilde{\sigma}_2 & -\tilde{\sigma}_1 \end{pmatrix}^2 = 2\tilde{\sigma}^2\delta^A_B \ , \tag{3.32}$$

and

$$\tilde{\sigma}^{\alpha\beta}\tilde{h}_{\alpha\beta} = \tilde{\sigma}^{AB}\delta_{AB} = 0 \ . \tag{3.33}$$

Note that although $\tilde{\sigma}_1$ and $\tilde{\sigma}_2$ are dependant on the choice of basis, $\tilde{\sigma}$ is not.

The equation of motion for $\tilde{\theta}$ can be found by differentiating it along the geodesic curve

$$\frac{\mathrm{d}\tilde{\theta}}{\mathrm{d}\lambda} = k^\mu\nabla_\mu\nabla_\nu k^\nu = -\frac{1}{2}\tilde{\theta}^2 - 2\tilde{\sigma}^2 - R_{\mu\nu}k^\mu k^\nu \tag{3.34}$$

where the Riemann curvature tensor definition (2.23) and the geodesic equation $k^\mu\nabla_\mu k^\nu = 0$ have been used as in the three-dimensional case (2.63). The source term can be written using (2.34), (2.31) and (3.3) as

$$R_{\mu\nu}k^\mu k^\nu = 8\pi G\omega^2\left(\rho + p + 2q_\mu e^\mu + \pi_{\mu\nu}e^\mu e^\nu\right) \ . \tag{3.35}$$

Note that the cosmological constant does not contribute to this term, as it can only enter into the expression of $R_{\mu\nu}$ in terms that contain $g_{\mu\nu}$, and since k^μ is a null vector, these terms vanish. The right hand side of equation (3.34) is always negative if the null energy condition holds, which is true for example in the ΛCDM cosmology. In these cases the expansion rate of the area of a null geodesic bundle always decreases. This leads to the focusing theorem (see eg. [52], page 134), which states that for a source and an observer separated by some affine parameter distance, the angular diameter distance is largest for the case where there is no matter between them as long as there are no caustics along the geodesic.

The equation of motion for the shear matrix can be derived by considering the derivative of $\tilde{B}_{AB}$ (note that it is a scalar!),

$$\begin{aligned}
\frac{\mathrm{d}}{\mathrm{d}\lambda}\tilde{B}_{AB} &= k^\mu\nabla_\mu s^\alpha_A s^\beta_B\nabla_\alpha k_\beta && (3.36)\\
&= s^\alpha_A s^\beta_B\left[-(\nabla_\alpha k^\mu)(\nabla_\mu k_\beta) - R_{\beta\nu\alpha\mu}k^\mu k^\nu\right] && (3.37)\\
&= s^\alpha_A s^\beta_B\left[-\tilde{B}_\alpha{}^\mu\tilde{B}_{\mu\beta} - R_{\alpha\mu\beta\nu}k^\mu k^\nu\right] && (3.38)\\
&= -\tilde{B}_A{}^C\tilde{B}_{CB} - R_{\alpha\mu\beta\nu}s^\alpha_A s^\beta_B k^\mu k^\nu && (3.39)\\
&= -\frac{1}{4}\tilde{\theta}^2\delta_{AB} - \tilde{\theta}\tilde{\sigma}_{AB} - \tilde{\sigma}_A{}^C\tilde{\sigma}_{CB} - R_{\alpha\mu\beta\nu}s^\alpha_A s^\beta_B k^\mu k^\nu && (3.40)\\
&= -\frac{1}{4}\tilde{\theta}^2\delta_{AB} - \tilde{\theta}\tilde{\sigma}_{AB} - \tilde{\sigma}^2\delta_{AB} - R_{\alpha\mu\beta\nu}s^\alpha_A s^\beta_B k^\mu k^\nu \ . && (3.41)
\end{aligned}$$

Taking the trace gives (3.34) and taking the traceless part gives

$$\frac{\mathrm{d}}{\mathrm{d}\lambda}\tilde{\sigma}_{AB} = -\tilde{\theta}\tilde{\sigma}_{AB} - C_{\alpha\mu\beta\nu}s^\alpha_A s^\beta_B k^\mu k^\nu \ , \tag{3.42}$$

where the traceless piece of the source term is proportional to the Weyl tensor.

The null expansion rate $\tilde{\theta}$ can be used to express the angular diameter distance. From its definition follows that (see e.g. [31], page 52)

$$\tilde{\theta} = \frac{1}{A}\frac{\mathrm{d}A}{\mathrm{d}\lambda} \tag{3.43}$$

where A is the cross sectional area of the beam. Using the definition of the angular diameter distance, (3.11), we can write this as

$$\tilde{\theta} = \frac{1}{2D_A}\frac{\mathrm{d}D_A}{\mathrm{d}\lambda}. \tag{3.44}$$

Equation (3.34) can also be written in terms of D_A

$$\frac{\mathrm{d}^2 D_A}{\mathrm{d}\lambda^2} + \left(\tilde{\sigma}^2 + \frac{1}{2}R_{\mu\nu}k^\mu k^\nu\right) D_A = 0\ . \tag{3.45}$$

3.5 Observations

This section covers some observations in cosmology, which are particularly important for the topic of this thesis.

3.5.1 Type Ia supernovae

A supernova is an exploding star [58]. They are classified based on the properties of their spectra. Those supernovae that show no traces of hydrogen absorption lines are called type I, and those that have an absorption line from ionized silicon are called type Ia, which are the ones that are most relevant for cosmology. All other supernovae are formed from a core collapse process, where the star's radiation pressure is no longer able to counteract the gravitational collapse, and an uncontrolled implosion starts. On the other hand, type Ia supernovae are thought to originate from a runaway fusion reaction that ignites after a white dwarf star has acquired enough matter from another star. There are two possible scenarios for their formation [59]. First, in a binary system with a white dwarf and a red giant, the red giant can leak matter onto the white dwarf, increasing the gravitational force until the Fermi degeneracy pressure is no longer able to resist the gravitational pull. At this point the white dwarf starts collapsing until nuclear fusion re-ignites. In a normal star, the fusion process is regulated by radiation pressure, but the white dwarf is so dense that radiation pressure cannot do this any more, so the fusion process spreads like a wildfire on a stellar scale. Second, if two white dwarf stars collide and merge, this can also re-ignite the fusion process, leading to a similar end result. Previously it was believed that the first process was responsible for all type Ia supernovae, but recently it has been proposed that a significant fraction of them could be generated via the second process.

The reason why type Ia supernovae are a crucial cosmological probe is that they are *standardisable* candles. Standardisable means that their relative intrinsic luminosities can be found by analysing their light curves, that is the time-evolution of their spectra. Once the relative intrinsic luminosities are known, one can calculate the relative luminosity distances. If in addition the redshift of the supernova has been measured, one can fit the measured (D_L, z)-pairs to the curve $D_L(z)$ predicted by the model, thus constraining the model parameters. The breakthrough happened in 1998, when two independent groups [8, 9] concluded that the expansion of the universe is accelerating. This result has since been corroborated by many groups (e.g. [60, 61, 62, 63, 64, 65, 66]), measuring supernovae independently in different redshift ranges and different parts of the sky, and the story seems to check out.

There are some potential pitfalls in the systematics of supernova analysis, however. As previously mentioned, it is currently unknown whether there are more than one possible mechanisms

for triggering a type Ia supernova, and whether the different mechanisms lead to a similarly standardisable light curves. If there were two different population of supernovae with different relation between the light curve and their intrinsic luminosity, that would jeopardise the conclusions that have been reached so far. Another problem is that the relation between light curves and intrinsic luminosity is not well understood at the present time [67]. Different light curve fitters give results that differ by a statistically significant amount, and it is not yet clear which of them one should believe, if any. Finally, often the supernova analyses rely heavily on the FRW spacetime and its distance-redshift relation (3.9). There have been a few proposals for testing the applicability of the distance-redshift relation of the FRW model [68, 69, 70], but then the constraining power of the data is diminished greatly, as one also needs the first derivative of the distance and independent measurement of the expansion rate $H(z)$, both of which are hard to measure.

For the testing of the FRW relation, we can differentiate equation (3.9) to find the curvature k in terms of the metric and its derivatives. Defining $D \equiv (1+z)D_A$, this gives

$$k = \frac{1 - H(z)^2 D'(z)^2}{D(z)^2} \ . \tag{3.46}$$

In the FRW model this expression is constant for all redshifts and sources, but in general it's not, and in general we can take this relation to be the definition of a function $k(z)$. If the universe is close to FRW, then k is constant or close to a constant whereas if $k(z)$ varies greatly, the FRW distance-redshift relation (3.9) does not describe distances in the real universe well. To see if $k(z)$ remains constant, a possible quantity to study is the derivative of $k(z)$, which can be written as [68]

$$\mathscr{C} \equiv -\frac{D^3}{2D'}k' = 1 + H^2(DD'' - D'^2) - HH'DD' \ . \tag{3.47}$$

3.5.2 Cosmic Microwave Background

The Cosmic Microwave Background (CMB) is a redshifted image of the universe from the time when its temperature was $\sim$ 3000K [72, 73, 74]. Today its temperature is $\sim$ 2.7K, so the photons have redshifted by an overall factor of $z \sim 1090$. After removing all of the noise from foreground sources, the photon temperature is still not completely uniform, but it contains fluctuations that arise due to the inhomogeneity of the universe. The largest relative fluctuation is the dipole that arises from the relative motion of the Earth (or the satellite!) with respect to the CMB. The dipole fluctuation is of the order $\frac{\Delta T}{T} \sim 10^{-3}$ whereas the fluctuations on smaller scales are considerably smaller, with a root mean square fluctuation of the order of $\frac{\Delta T}{T} \sim 10^{-5}$. The CMB signal can be also split into a primary part and a secondary part. The primary signal originates from the surface of last scattering at $z \sim 1090$ whereas the secondary signal is generated during the photons' journey through the universe. The secondary signal is generated in two distinct ways: by the photons scattering off charged particles, and by cosmic structures along the photons line of sight and their gravitational influence. The primary signal is of great interest in cosmology, as it contains information about the very early universe, mapping the initial conditions that sparked the formation of cosmic structure. It is also an order of magnitude higher than the secondary signal. The secondary scattering signal, and especially the Sunyaev-Zel'dovich effect, have important applications in cosmology and in astrophysics. In this thesis however, the secondary gravitational signal will be the main focus.

The temperature anisotropies produced by first-order metric perturbations are generated via the Integrated Sachs-Wolfe (ISW) effect [75], the anisotropies that come from second order effects are generated via the Rees-Sciama (RS) effect [76], and finally some of the primary CMB anisotropies are modified by gravitational lensing. On large scales where perturbation theory

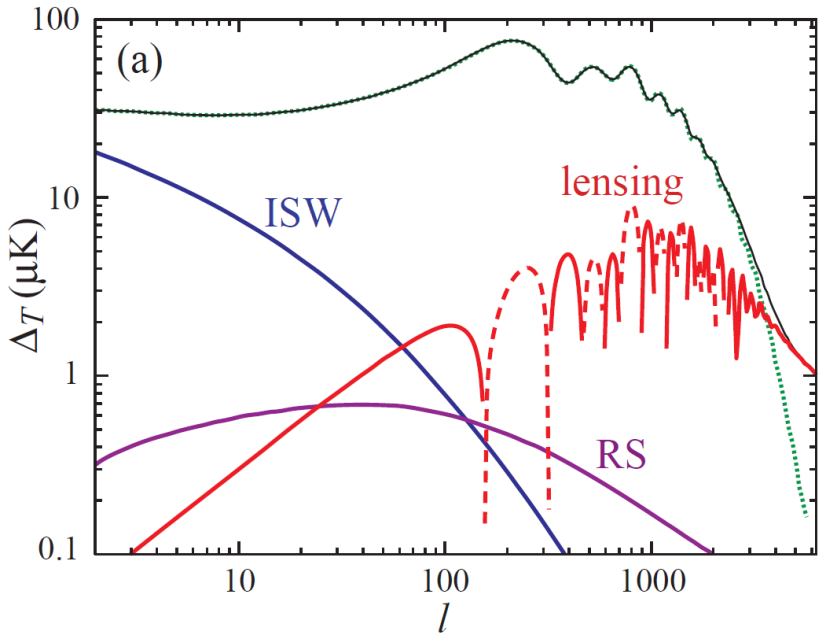

Figure 3.1: The CMB temperature fluctuations split into the primary anisotropy, ISW effect, RS effect and gravitational lensing. The x-axis shows the multipole l (see (3.48)) and Y-axis is the expected temperature fluctuation for that multipole. Figure from [71].

holds to high precision, the ISW effect dominates over the RS effect and lensing, whereas on small scales, lensing dominates over the RS effect, which in turn is greater than the ISW effect. The detailed behaviour of the three signals as a function of scale is show in Figure 3.1. Lines of sight that contain less matter than on average tend to be colder and lines of sight that contain more matter tend to be hotter – voids produce a cold spot and superclusters produce a hot spot in the CMB. There have been attempts to measure this from the CMB by seeing how the CMB temperature signal is correlated with large-scale structure [77, 78].

For any Gaussian random field on a sphere, the angular power spectrum is a convenient way to express the statistical properties of the field. Any function $f(\theta, \phi)$ can be expanded in terms of the spherical harmonics Y_{lm},

$$f(\theta,\phi) = \sum_{l>0} \sum_{m=-l}^{l} a^f_{lm} Y_{lm}(\theta,\phi) \tag{3.48}$$

$$a^f_{lm} = \int \mathrm{d}\Omega \; Y^*_{lm}(\theta,\phi) \; f(\theta,\phi) \; , \tag{3.49}$$

where the coefficients a^f_{lm} do not depend on the angles. If f is a Gaussian random field, then each a^f_{lm} is an independent Gaussian random variable with zero mean. The power spectrum C^{ff}_l is defined as

$$C^{ff}_l \equiv \frac{1}{2l+1} \sum_{m=-l}^{l} |a^f_{lm}|^2 \; . \tag{3.50}$$

For a given multipole number l, the power spectrum tells us the amplitude of typical fluctuations on that scale. Small multipole numbers correspond to large scales and vice versa, with the multipole $l = 100$ corresponding roughly to an angular scale of 1° on the sky and the dipole being $l = 1$. If the field is Gaussian, then the power spectrum fully characterises the correlations of the field.

In addition to the temperature and polarization power spectra, there has been some interest in other kinds of ways to characterise the fluctuations in the CMB. Primordial non-Gaussian fluctuations have been searched for extensively but have not been found so far [79]. There have been claims that the different sky hemispheres contain different amount of fluctuations on small scales [80, 81, 82], but it seems at least some of the difference can be explained via known data analysis effects [83]. A local non-Gaussian feature has also been identified from the CMB, named *the Cold Spot* [84]. This feature was discussed in paper **II** and it will be covered further in Section 5.1.

3.5.3 Gravitational lensing

Gravitational lensing is conventionally split into strong and weak lensing. Strong lensing [85, 86] (see [52], page 1 for a detailed historical account) is characterised by the lens producing several images of the source, whereas weak lensing only changes the brightness, surface area and shape of the source image. Gravitational lensing is used to find information about the lensing structure. In the case of strong lensing, this is typically a cluster of galaxies, where lensing can reveal the distribution of dark matter very precisely. In the case of weak lensing, the source is all of the matter fluctuations in the line of sight from the source to the observer. Thus weak lensing is arguably the more interesting topic for cosmology.

Weak lensing analysis can be applied to different kinds of sources. In the case of galaxies, the problem is that galaxies come in all kinds of different sizes, shapes and brightnesses. In particular, a galaxy can be oriented in whatever way with respect to us, so it is difficult to say whether it looks elongated because it has been lensed by an object on the line of sight, or whether it is just aligned that way. However, the average shape of a galaxy is a sphere. In other words, there should be no preferred way the galaxies are intrinsically aligned with respect to us. Detecting weak lensing reliably from a single source galaxy is nearly impossible. However, one can look at the lensing of a large number of galaxies [87, 88, 89, 90] and the correlations of nearby sources to see the overall lensing signal. The CMB can also be used as the source in weak lensing [91]. The data from the Planck satellite has been used to construct the integrated lensing potential over the whole sky [92].

In the study of weak lensing, the deformation of the source image is described using the weak lensing formalism, with slightly different parameters than the covariant θ and σ_{AB}. The relative change in the beam cross section is described by the amplification matrix (see e.g. [52], page 162)

$$\mathcal{A}^{A}{}_{B} = \begin{pmatrix} 1-\kappa-\gamma_1 & \gamma_2 \\ \gamma_2 & 1-\kappa+\gamma_1 \end{pmatrix} , \tag{3.51}$$

that is the Jacobian of the lens map. The convergence κ describes the change in beam area and the integrated shear γ describes the deformation of the beam cross section. Finally the magnification

$$\mu = \det(\mathcal{A}^{-1}) = \left[(1-\kappa)^2 - \gamma^2\right]^{-1} \tag{3.52}$$

gives the change in luminosity relative to the homogeneous FRW background with $\gamma \equiv \sqrt{\gamma_1^2+\gamma_2^2}$. In the weak lensing limit, $\kappa \ll 1$ and $\gamma \ll 1$, the weak lensing quantities can be related to the covariant quantities (3.23) via

$$\mu = \frac{\bar{D}_A^2}{D_A^2} \simeq 1-2\kappa , \qquad \gamma_i \simeq \int \mathrm{d}\lambda \tilde{\sigma}_i , \tag{3.53}$$

where $\bar{D}_A$ is the angular diameter distance in the background FRW universe, so

$$\frac{\Delta D_A}{\bar{D}_A} \equiv \frac{D_A - \bar{D}_A}{\bar{D}_A} \simeq -\kappa . \tag{3.54}$$

Another common way to represent the variables μ, κ and σ is the lensing potential Ψ, defined via

$$\mathcal{A}_{AB} = \delta_{AB} - \partial_A \partial_B \Psi \ . \tag{3.55}$$

The lensing potential can be calculated as a weighed integral of the first order gravitational potential [91].

Chapter 4

Inhomogeneous spacetimes

In addition to the homogeneous FRW spacetime described in section 2.2, other solutions can be found to the Einstein equation. Exact analytic solutions can be found if the energy-momentum tensor is simple and initial conditions have some symmetries. Perturbative solutions can be found if the metric and its derivatives are close to a simpler solution everywhere. Finally, some spacetimes can be joined together to produce a more complicated and less symmetric solution. This chapter goes through some of these possibilities.

4.1 Perturbations in FRW

In the concordance model, the universe is described with a perturbed FRW metric. The Einstein equation can be solved perturbatively as long as the metric perturbations and their derivatives are small. In this case, the evolution of the unperturbed background does not depend on the perturbations. After the background evolution is known, the evolution of perturbations can be solved for the first order, second order and so on until paper runs out. The solution gets messy fairly quickly, but a second order solution in a flat FRW background has been written down.

4.1.1 The metric and its evolution

Here we should use conformal time $\mathrm{d}\eta = \mathrm{d}t/a$ as the time coordinate, and prime $'$ stands for $\partial/\partial\eta$. The perturbed metric can be written as

$$g_{\mu\nu} = a^2 \left(\hat{g}^{(0)}_{\mu\nu} + \hat{g}^{(1)}_{\mu\nu} + \frac{1}{2}\hat{g}^{(2)}_{\mu\nu} + \dots \right) , \tag{4.1}$$

where $\hat{g}^{(0)}_{\mu\nu}$ is the Minkowski metric. The metric components can be written as (following [93, 94])

$$\hat{g}_{00} = -1 + 2\psi^{(1)} + \psi^{(2)} + \dots \tag{4.2}$$

$$\hat{g}_{0i} = z_i^{(1)} + \frac{1}{2} z_i^{(2)} + \dots \tag{4.3}$$

$$\hat{g}_{ij} = \delta_{ij}(1 - 2\phi^{(1)} - \phi^{(2)} + \cdots) + \chi_{ij}^{(1)} + \frac{1}{2}\chi_{ij}^{(2)} + \cdots , \tag{4.4}$$

and the observer four-velocity can be written as

$$u^\mu = \frac{1}{a}\left(\delta^\mu_0 + v^{(1)\mu} + \frac{1}{2} v^{(2)\mu} \dots \right) . \tag{4.5}$$

The time components can be found from the normalization $u_\mu u^\mu = -1$ to be

$$v^{(1)0} = -\psi^{(1)} \tag{4.6}$$

$$v^{(2)0} = -\psi^{(2)} + 3(\psi^{(1)})^2 + 2z_i^{(1)} v^{(1)i} + v_i^{(1)} v^{(1)i} \tag{4.7}$$

$$\vdots \tag{4.8}$$

There is a complication in doing perturbation theory in general relativity, which is that there is no unique mapping between points in the background and perturbed spacetimes. The choice of mapping is called the *gauge* choice, which can be made via a small coordinate transformation $x^\mu \to x^\mu + \zeta^\mu$, called the gauge transformation. Although perturbed quantities depend on the gauge choice, since the choice defines what is background and what is perturbation, physics should remain independent of the coordinates. Some of the degrees of freedom in the metric are not physical, but are related to the choice of the gauge. In first order perturbation theory, the gauge transformations are relatively simple and textbook material (e.g. [95]). The metric perturbation has ten degrees of freedom, and four of them correspond to the choice of ζ^μ, leaving six physical degrees of freedom. Second order brings some complications [96], but the same idea still applies: the gauge transformation can be chosen so that some of the metric perturbations vanish. This thesis has results calculated in the Poisson gauge, where the coordinate mapping is chosen so that $\partial_i z^{(n)i} = 0$ and $\partial_i \chi^{(n)ij} = 0$ for all orders n. Another example of a possible choice is the synchronous gauge, where $\psi^{(n)} = 0$ and $z_i^{(n)} = 0$. First-order perturbation theory is often done in the conformal Newtonian gauge, which has $z_i^{(1)} = \chi_{ij}^{(1)} = 0$. This condition is a stronger version of the Poisson gauge, as it also requires that there are no vector or tensor modes in the solution. Conformal Newtonian gauge cannot be constructed at second order, as these modes are generated automatically from the first order perturbations.

In the Poisson gauge, we can write out some parts of the first-order solution in terms of a function of conformal time $P(\eta)$ and a function of location $F(\mathbf{x})$ (see [97, 98, 99] for the full solution)

$$\psi^{(1)} = \phi^{(1)} = -\frac{1}{2}\left(1 - \frac{a'}{a}P'\right)F \tag{4.9}$$

$$v^{(1)i} = \frac{1}{2}P'\partial_i F \ . \tag{4.10}$$

These pieces of the metric will give the dominant contribution to the temperature signal calculated in the next section. The function P is the solution of the equation

$$P'' + \frac{2a'}{a}P' - 1 = 0 \ . \tag{4.11}$$

It is a second-order differential equation, so it has two independent solutions, but we are only interested in the growing solution. The potential function $F(\mathbf{x})$ is related to the first order density contrast, so to specify it, one needs to specify the density profile of the feature under study. For a radial density profile, the result is [100]

$$F(r) = \frac{3\Omega_m \bar{H}_0^2}{(1 - a'P'/a)|_{a=1}}\left[\int_0^r \frac{r'^2}{r}\delta(r')\mathrm{d}r' + \int_r^\infty r'\delta(r')\mathrm{d}r'\right] \ , \tag{4.12}$$

where $\delta(r) \equiv \rho/\bar{\rho} - 1$ is the density contrast. The second order solution can also be written out in terms of P and F [99], but the solution is much more complicated so the details are not included here.

4.1.2 Temperature perturbations

The photon wave vector can also be expanded

$$k^\mu = k^{(0)\mu} + k^{(1)\mu} + k^{(2)\mu} + \dots \tag{4.13}$$

with the unperturbed wave vector

$$k^{(0)\mu} = (1, -e^i) \ . \tag{4.14}$$

The photon temperature $T = \bar{T} + \Delta T^{(1)} + \Delta T^{(2)} + \dots$ can be calculated using (3.2) (see [94] for the full calculation)

$$\frac{\Delta T^{(1)}}{\bar{T}} = \psi_S^{(1)} - \psi_O^{(1)} - v_S^{(1)i} e_i + v_O^{(1)i} e_i - I_1 \ , \tag{4.15}$$

with

$$I_1 = \int_{\lambda_O}^{\lambda_S} \mathrm{d}\lambda \frac{\mathrm{d}}{\mathrm{d}\lambda} \left(\psi^{(1)} + \phi^{(1)} + z_i^{(1)} e^i - \frac{1}{2} \chi_{ij}^{(1)} e^i e^j \right) \ . \tag{4.16}$$

Here again O and S stand for observer and source, respectively. Choosing the conformal Newtonian gauge, $z_i^{(n)} = \chi_{ij}^{(n)} = 0$, gives the familiar Integrated Sachs Wolfe formula [72, 73]

$$\frac{\Delta T_{\mathrm{ISW}}}{\bar{T}} = \int_{t_S}^{t_O} \mathrm{d}t \ (\dot{\psi}^{(1)} + \dot{\phi}^{(1)}) = 2 \int_{t_S}^{t_O} \mathrm{d}t \ \dot{\psi}^{(1)} \ . \tag{4.17}$$

The second order temperature perturbation is a lot more complicated, so it will not be shown here in its full glory. The one piece worth mentioning is the counterpart to (4.17), the term responsible for the Rees-Sciama effect

$$\frac{\Delta T_{\mathrm{RS}}}{\bar{T}} = \frac{1}{2} \int_{t_S}^{t_O} \mathrm{d}t \ (\dot{\psi}^{(2)} + \dot{\phi}^{(2)}) \ . \tag{4.18}$$

The ISW effect is produced by a varying first order gravitational potential $\psi^{(1)}$. In the flat FRW solution with only dust, $\Omega_m = 1$, $\Omega_\Lambda = 0$, the function $P = \frac{2}{5a^2H^2}$ and $P' = \frac{2}{5aH}$. Therefore $\psi^{(1)}$ remains constant so in this case the ISW contribution vanishes identically. In a model with dust and dark energy, the potential decays. As a photon climbs on a potential hill (corresponding to a void), it loses energy and as it falls out, it gains some of the energy back. Since the potential has decayed during its travel time, it does not gain everything it lost back, leading to net cooling of the photons. Likewise, decaying potential wells cause the photons to gain some extra energy, making them hotter.

4.2 The Lemaître-Tolman-Bondi solution

The number of symmetries in the FRW solution limits the number of permitted solutions. By relaxing the number of symmetries, more complicated solutions are allowed. The Lemaître-Tolman-Bondi (LTB) metric is the most general spherically symmetric dust solution to the Einstein equation [101, 102, 103, 104]. The LTB metric includes the Schwarzschild metric (in synchronous coordinates) and the FRW metric as special cases, and in addition to these, a large number of less symmetric solutions are possible.

4.2.1 The LTB metric

The metric has the form

$$\mathrm{d}s^2 = -\mathrm{d}t^2 + X^2(t,r)\mathrm{d}r^2 + R^2(t,r)(\mathrm{d}\theta^2 + \sin^2(\theta)\mathrm{d}\phi^2) \tag{4.19}$$

in synchronous coordinates. The energy-momentum tensor can be written in the same coordinates as

$$T^{\mu\nu} = \rho_M(t,r)\delta^\mu_0\delta^\nu_0 - \rho_\Lambda g^{\mu\nu} \ , \tag{4.20}$$

where the first term is contributed by dust and the second term by cosmological constant, $8\pi G\rho_\Lambda \equiv \Lambda$. For simplicity we will denote dust density as ρ from now on and use Λ for cosmological constant. The connection coefficients and the components for Riemann, Ricci, Weyl and Einstein tensors are calculated in Appendix A. Time derivatives are denoted with a dot and radial derivatives with a prime.

The vanishing of the off-diagonal Einstein tensor components (A.19) leads to a relation between the metric functions,

$$\frac{\dot{X}}{X} = \frac{\dot{R}'}{R'} \ , \tag{4.21}$$

if $R' \neq 0$ and integration with respect to time leads to

$$X = \frac{R'}{\sqrt{1+2E(r)}} \ , \tag{4.22}$$

where $\sqrt{1+2E(r)}$ is the integration constant, and $E(r)$ is a function that is related to the spatial curvature of a shell at radius r. The radial component of the Einstein equation (A.21) is

$$2R\ddot{R} + \dot{R}^2 = 2E + \frac{1}{3}\Lambda R^2 \ , \tag{4.23}$$

which can be integrated once in terms of t to yield

$$\dot{R}(t,r)^2 = 2E(r) + \frac{2M(r)}{R(t,r)} + \frac{1}{3}\Lambda R^2(t,r) \ , \tag{4.24}$$

where $M(r)$ is another function that does not depend on time. Substituting this into the Einstein equation time component gives

$$\rho = \frac{M'}{4\pi G R^2 R'} \ . \tag{4.25}$$

The volume element of a spatial hypersurface is

$$\mathrm{d}V = \frac{R^2 R'}{\sqrt{1+2E}}\sin(\theta)\mathrm{d}r\mathrm{d}\theta\mathrm{d}\phi \ , \tag{4.26}$$

so (4.25) means that $M(r)$ corresponds almost to the integrated mass inside a spherical shell of radius r, apart from the additional factor of $\sqrt{1+2E}$ in the volume element and a factor of Newton's constant.

The solution of (4.24) can be written as an integral (note the similarity to the FRW case, (2.43))

$$t - t_B(r) = \int_0^{R(t,r)} \frac{\mathrm{d}R}{\sqrt{\frac{2M}{R} + 2E + \frac{1}{3}\Lambda R^2}} \ , \tag{4.27}$$

and then inverting the integral equation numerically to find the solution $R(t,r)$. Here $t_B(r)$ is the bang time function, which tells the time of the initial singularity, $R(t_B(r),r) = 0$. It is the third function set by boundary and initial conditions, and these three functions specify the solution completely. Later we will consider some requirements that these functions must have to produce a physical universe, but at this time, they can be considered arbitrary. In general, equation (4.27) must be integrated numerically, but in some special cases, a simpler solution can be found. Some solutions are described in detail in sections 4.2.5 and 4.2.6.

4.2.2 Expansion, shear and spatial curvature

The dust in the LTB model moves on geodesics $u^\mu = (1, 0, 0, 0)$. The volume expansion rate is

$$\theta = \nabla_\mu u^\mu = \Gamma^\mu_{\mu 0} = \frac{\dot{R}'}{R'} + \frac{2\dot{R}}{R} = H_\parallel + 2H_\perp \ , \tag{4.28}$$

where the radial and perpendicular to radial expansion rates have been defined. The shear tensor is

$$\sigma^\mu{}_\nu = \mathrm{diag}\,(0, 2/3, -1/3, -1/3)\left(H_\parallel - H_\perp\right) \ , \tag{4.29}$$

and the vorticity tensor vanishes. Even in a model with a monotonically growing R, the expansion rate can locally be negative as $H_\parallel$ can be negative. In such a case, the surface area of the shell increases, but the distance between two nearby shells decreases, leading to an overall decrease in the volume of an infinitesimally thin shell. The spatial Ricci scalar is

$${}^{(3)}R = -2\frac{(ER)'}{R^2 R'} \ . \tag{4.30}$$

Typically the spatial Ricci scalar is positive in overdense regions and negative in underdense regions.

4.2.3 Choice of functions

The time evolution of density and curvature contrasts in an LTB model depends on the choice of functions $t_B(r)$ and $E(r)$. A gradient in t_B generates a decaying mode in both curvature and density, scaling $\propto t^{-1}$ in a model with no cosmological constant. A gradient in E generates a growing mode in density, which scales $\propto t^{2/3}$ in a model with no cosmological constant [105]. If $t_B' \neq 0$, density contrast becomes infinite at the time of the bang, whereas all models with $t_B' = 0$ become homogeneous as $t \to t_B$. From CMB observations it is known that the universe was highly homogeneous at the time of the CMB decoupling. This puts considerable constraints on models with $t_B' \neq 0$. The coordinate r has no physical meaning, and the solution does not change under changes $r \to f(r)$ if f is monotonic. Up to the normalisation, the choice of $M(r)$ is degenerate with the choice of r.

4.2.4 Shell crossings

Since the source matter in the LTB model is dust, there is no pressure and therefore nothing to stop gravitational collapse. If a situation arises where an inside shell is expanding faster than an outside shell, $H_\parallel < 0$, they may collide when $R' \to 0$. If at this point $M' \neq 0$, the density (4.25) diverges and a hydrodynamical shell-crossing singularity is formed [106, 107]. Although the shell crossing is a real naked curvature singularity, it is a weak singularity in the sense that a spaceman travelling through it would not get crushed [108, 109], unlike for example a black hole or the Big Bang.

The shell crossings are a feature of the mathematical description of pressureless ideal fluid. In the real universe, there would be pressure gradients and particle collisions that can ultimately stop the shell crossing from happening. However, it is nonetheless a fundamental feature of these models that must be taken into account, and that must in practice be avoided. The full conditions to avoid shell crossings entirely are discussed in [106]. In particular, a model with $R' > 0$ and $E \geq 0$ must also satisfy $t_B' \leq 0$, $E' \geq 0$ and $M' \geq 0$. For cosmological applications these conditions are very limiting. In practice it's better to consider models that do not develop a shell crossing during the time scale of interest (e.g. the age of the universe). As long as the shell crossings happen in the future, there is no need to worry about them as we can easily imagine

that in the real universe, pressure would stop the collapse before a shell crossing occurred. By tuning the model so that $R' \neq 0$ for the time interval of interest, we do not need to worry about shell crossings. There is another possibility, if we allow $R' = 0$ at specific constant coordinate radii r_i, where also $M' = 0$ and $\lim_{r\to r_i} |M'/R'| < \infty$. Then the density will remain finite if also $E \to -1/2$, otherwise a thin singular shell is formed.

4.2.5 Simple cases

If one or more of the terms on the right-hand side of (4.24) vanishes, the integral simplifies to something that can be expressed in terms of elementary functions. For simplicity, we only consider here cases where $\Lambda \geq 0$. Here are some of the cases that are used later. In the cases where two of the terms are zero, the equation can be separated and immediately integrated

$$R(t,r) = \begin{cases} \left(\frac{9}{4}M(r)(t - t_B(r))^2\right)^{1/3} & \text{for } E = 0,\ \Lambda = 0 \\ \sqrt{2E(r)}(t - t_B(r)) & \text{for } M = 0,\ \Lambda = 0 \\ R(t_0,r)\exp\left(\sqrt{\frac{\Lambda}{3}}(t - t_0)\right) & \text{for } E = 0,\ M = 0 \end{cases} \tag{4.31}$$

Note that the function t_B does not enter on the last row, as R is never zero in such a case. Instead R is given in terms of its value on some other (arbitrary) time t_0.

In the case $E = 0$, the solution is

$$R(t,r) = \left[\frac{6M}{\Lambda}\sinh^2\left(\sqrt{\frac{3\Lambda}{4}}(t - t_B)\right)\right]^{1/3} . \tag{4.32}$$

In the case $M = 0$ and $E > 0$, the solution is

$$R(t,r) = \sqrt{\frac{6E}{\Lambda}}\sinh\left[\sqrt{\frac{\Lambda}{3}}(t - t_B)\right] . \tag{4.33}$$

The FRW solution can be found as a special case for the LTB metric, corresponding to the choice of

$$t_B(r) = \text{constant}, \quad M(r) = \frac{4\pi r^3}{3}\rho_0, \quad E(r) = -\frac{1}{2}kr^2 , \tag{4.34}$$

in which case the solution simplifies to $R(t,r) = a(t)r$.

The Kottler metric,

$$\mathrm{d}s^2 = -A(R)\mathrm{d}T^2 + \frac{1}{A(R)}\mathrm{d}R^2 + R^2\mathrm{d}\Omega^2 , \tag{4.35}$$

with $A(R) = 1 - \frac{R_s}{R} - \frac{1}{3}\Lambda R^2$ and $R_s = 2GM$ is the generalisation of the Schwarzschild metric to include the cosmological constant. Although in these coordinates it does not look like the LTB metric, a coordinate transformation can be made to bring the metric into the LTB form, see e.g. [110]. The Lemaître coordinates are

$$\mathrm{d}t = \mathrm{d}T + \sqrt{1 - A}\frac{\mathrm{d}R}{A} , \quad \mathrm{d}r = \mathrm{d}T + \frac{1}{\sqrt{1 - A}}\frac{\mathrm{d}R}{A} , \tag{4.36}$$

and plugging them into the metric gives

$$\mathrm{d}s^2 = -\mathrm{d}t^2 + [1 - A(R(t,r))]\,\mathrm{d}r^2 + R^2(t,r)\mathrm{d}\Omega . \tag{4.37}$$

Solving for $R(t,r)$ gives

$$R(t,r) = \left[\frac{3R_S}{\Lambda}\sinh^2\left(\sqrt{\frac{3\Lambda}{4}}(t-r)\right)\right]^{1/3} , \tag{4.38}$$

from which it can be seen that the solution matches to LTB with $E(r) = 0$, $M = R_S/2$ constant and $t_B(r) = -r$.

4.2.6 The classic case with no cosmological constant

The case $\Lambda = 0$ is the classic case that has been often studied. In this case there exists a parametric solution

$$R(t,r) = \frac{M}{2|E|}(1-\cos\eta), \quad \eta - \sin\eta = \frac{(2|E|)^{3/2}}{M}(t-t_B), \text{ for } E<0 \tag{4.39}$$

$$R(t,r) = \frac{M}{2E}(\cosh\eta - 1), \quad \sinh\eta - \eta = \frac{(2E)^{3/2}}{M}(t-t_B), \text{ for } E<0 . \tag{4.40}$$

We can also find analytic forms for the radial derivatives. Differentiating R once with respect to r leads to

$$R' = \frac{M}{2E}\left[\left(\frac{M'}{M} - \frac{E'}{E}\right)(\cosh\eta - 1) + \eta'\sinh\eta\right] \tag{4.41}$$

$$\equiv \frac{M}{2E}\left[\alpha(\cosh\eta - 1) + \eta'\sinh\eta\right] \tag{4.42}$$

and differentiating the equation for η gives

$$\eta' = \frac{1}{\cosh\eta - 1}\frac{(2E)^{3/2}}{M}\left[\left(\frac{3E'}{2E} - \frac{M'}{M}\right)(t-t_B) - t_B'\right] \tag{4.43}$$

$$\equiv \frac{1}{\cosh\eta - 1}\frac{(2E)^{3/2}}{M}\left[\beta(t-t_B) - t_B'\right] , \tag{4.44}$$

where the following functions have been introduced:

$$\alpha(r) = \frac{M'}{M} - \frac{|E|'}{|E|} \qquad \beta(r) = \frac{3|E|'}{2|E|} - \frac{M'}{M} . \tag{4.45}$$

Combining the two expressions above, we find that

$$R' = \alpha R + \dot{R}[\beta(t-t_B) - t_B'] . \tag{4.46}$$

This expression holds for all values of E with the convention that $E'/E = 0$ for $E = 0$, with the proof for $E < 0$ following exactly the same steps. The second derivative can be written similarly in the form

$$R'' = (\alpha' + \alpha^2)R + \left[\dot{R}(\alpha\beta + \beta') + \dot{R}'\beta\right](t-t_B) - \left[\dot{R}(\alpha+\beta) + \dot{R}'\right]t_B' - \dot{R}\,t_B'' . \tag{4.47}$$

4.2.7 Light propagation

Geodesic equation and redshift. The geodesic equation $k^\mu\nabla_\mu k^\nu = 0$ can be explicitly written out for a wave vector

$$k^\mu = \frac{\mathrm{d}x^\mu}{\mathrm{d}\lambda} = \left(\frac{\mathrm{d}t}{\mathrm{d}\lambda}, \frac{\mathrm{d}r}{\mathrm{d}\lambda}, \frac{\mathrm{d}\theta}{\mathrm{d}\lambda}, \frac{\mathrm{d}\phi}{\mathrm{d}\lambda}\right) , \tag{4.48}$$

but let us first note a few simplifications. The LTB solution has a killing vector $\eta^\mu = (\partial_\phi)^\mu$ so the quantity

$$c_\phi \equiv k_\mu \eta^\mu = k^\phi R^2 \sin^2\theta \tag{4.49}$$

is conserved, allowing immediately to solve the ϕ-component of the equation. Furthermore, due to full spherical symmetry, the coordinates can be always rotated so that k^μ lies in the plane with $\theta = \pi/2$ without loss of generality, so $k^\theta = 0$. Using (4.49) to eliminate k^ϕ, the remaining equations are

$$\frac{\mathrm{d}k^t}{\mathrm{d}\lambda} = -\frac{\dot{R}'}{R'}(k^t)^2 + \frac{c_\phi^2}{R^2}\left(\frac{\dot{R}'}{R'} - \frac{\dot{R}}{R}\right) = -(k^t)^2 H + \left[\frac{c_\phi^2}{R^2} - \frac{2(k^t)^2}{3}\right]\Sigma \tag{4.50}$$

$$\frac{\mathrm{d}k^r}{\mathrm{d}\lambda} = -2\frac{\dot{R}'}{R'}k^t k^r - \left[(1+2E)\frac{R''}{R} - E'\right](k^r)^2 + (1+2E)\frac{c_\phi^2}{R^3 R'} \ . \tag{4.51}$$

Finally, the null condition $k_\mu k^\mu = 0$ can be written out to solve for example k^r,

$$k^r = \pm\frac{\sqrt{1+2E}}{R'}\sqrt{(k^t)^2 - \frac{c_\phi^2}{R^2}} \ . \tag{4.52}$$

If the source and the observer are comoving with the dust, their four-velocities are $u^\mu = (1,0,0,0)$ and so the observer measures the redshift (3.2) of the light to be

$$1 + z = \frac{u_\mu k_S^\mu}{u_\mu k_O^\mu} = \frac{k_S^t}{k_O^t} \ . \tag{4.53}$$

If the geodesic equations are solved backwards in time from the observer to the source, then k_O^t is an initial constant and $1 + z \propto k_S^t$. If the geodesic equations are instead solved forwards, then k_S^t is the initial value and $(1+z)^{-1} \propto k_O^t$. Photon temperature scales as $T \propto 1 + z$ so the temperature fluctuation from the background can be calculated from

$$\frac{\Delta T}{\bar{T}}(\mathbf{n}, t) = 1 - (1 + z(\mathbf{n}, t))\,\bar{a}(t) \ , \tag{4.54}$$

where $\mathbf{n}$ is the direction of observation.

Sachs equations and distance. To solve the Sachs equations (3.34) and (3.42), we need to find expressions for their source terms. The expansion equation source term (3.35) is easy,

$$R_{\mu\nu}k^\mu k^\nu = 8\pi G\rho(k^t)^2 \ . \tag{4.55}$$

The shear equation source term $C_{\alpha\mu\beta\nu}s_A^\alpha s_B^\beta k^\mu k^\nu$ is slightly more complicated. We can choose one of the basis vectors to be $s_1^\alpha = (0, 0, 1/R, 0)$, which clearly satisfies the requirements (3.27) and (3.28). This gives

$$C_{\alpha\mu\beta\nu}s_1^\alpha s_1^\beta k^\mu k^\nu = \frac{1}{R^2}R_{\theta\mu\theta\nu}k^\mu k^\nu = \frac{c_\phi^2}{R^2}\left(\frac{3M}{R^3} - 4\pi G\rho\right) \ . \tag{4.56}$$

This choice corresponds to one of the principal axes of the transformation, so $\tilde{\sigma}_2$ remains zero. In a spherically symmetric solution, such a set of vectors can always be found (see [111] for explicit calculations).

4.2.8 The Szekeres solution

If the requirement of spherical symmetry is dropped, the solution is the Szekeres metric [112, 113], the most general known inhomogeneous dust solution,

$$\mathrm{d}s^2 = -\mathrm{d}t^2 + X^2(t,r,p,q)\mathrm{d}r^2 + \frac{R^2(t,r)}{\mathcal{E}^2(r,p,q)}\left(\mathrm{d}p^2 + \mathrm{d}q^2\right) \ . \tag{4.57}$$

The functions X and $\mathcal{E}$ satisfy

$$X(t,r,p,q) = \frac{\left|R' - R\frac{\mathcal{E}'}{\mathcal{E}}\right|}{\sqrt{\epsilon + 2E(r)}} \tag{4.58}$$

$$\mathcal{E}(r,p,q) = \frac{S(r)}{2}\left[\left(\frac{p-P(r)}{S(r)}\right)^2 + \left(\frac{q-Q(r)}{S(r)}\right)^2 + \epsilon\right] \ , \tag{4.59}$$

where the free functions E, P, Q and S depend only on the radial coordinate r and the constant ϵ can take values of -1, 0 or 1, called quasihyperbolic, quasiplanar and quasispherical cases, respectively. The names refer to the properties of the constant t and r surfaces. The quasihyperbolic case is discussed in e.g. [114] and the quasiplanar case in e.g. [115, 116]. The quasispherical case is the one most studied, as the the constant r surfaces are finite in that case, and so it can be more easily related to cosmology. The LTB metric is a special case of the quasispherical Szekeres solution with $\mathcal{E}' = 0$. Even in the general case, the equation of motion for R is exactly as in the LTB model, eq. (4.24).

4.3 Swiss Cheese

A Swiss Cheese model typically consists of an FRW background spacetime with spherical holes cut into it. A different, less symmetric solution, such as an LTB or Szekeres solution can be embedded into the hole. The original proposal by Einstein and Straus [117] was to embed Schwarzschild black holes into a dust FRW background, but this procedure can easily be generalised to joining together any two spacetimes that satisfy the Darmois junction conditions [118, 119]. As long as the holes are not overlapping, any number of them can be added onto the background to simulate the cosmic structure.

4.3.1 Junction conditions

Two pieces of spacetime $\mathscr{V}^+$ and $\mathscr{V}^-$ are joined together along a three-dimensional hypersurface Σ. The surface Σ can be spacelike, timelike or null; however, here only spacelike and timelike surfaces are considered for simplicity. The coordinates in these pieces are $x^\mu_\pm$ and the metric tensor components in these coordinates are $g^\pm_{\mu\nu}$. To form an atlas, the coordinates must overlap in an open set containing Σ, where the coordinates are denoted by x^μ. One way to define Σ is to construct a scalar field Φ that satisfies for all points $p \in \Sigma$, $\Phi(p) = 0$. Then the vector $n_\alpha = -\partial_\alpha\Phi$ is a normal vector to the surface. If the surface is spacelike or timelike, the vector can be trivially normalised so that $n^\alpha n_\alpha = \epsilon = \pm 1$. Let's define Φ as follows: it is the proper time along geodesics that intersect Σ orthogonally, with the convention that Φ is negative in $\mathscr{V}^-$ and positive in $\mathscr{V}^+$. In this case the normal vector is spacelike.

The four-metric can be written in terms of the Heaviside function $\Theta(\Phi)$, which has the value 1 for positive Φ, 0 for negative Φ and $\frac{1}{2}$ for $\Phi = 0$. Its derivative is the Dirac delta distribution $\delta(\Phi)$.

$$g_{\mu\nu} = \Theta(\Phi)g^+_{\mu\nu} + \Theta(-\Phi)g^-_{\mu\nu} \ . \tag{4.60}$$

In order for this to be a proper metric that is a valid solution of the Einstein equations, the geometric terms constructed from it must have a proper distributional form, so that no improper terms like $\Theta(\Phi)\delta(\Phi)$ can appear. The derivative of the metric is

$$\partial_\alpha g_{\mu\nu} = \Theta(\Phi)\partial_\alpha^+ g_{\mu\nu}^+ + \Theta(-\Phi)\partial_\alpha^- g_{\mu\nu}^- + \delta(\Phi)\left(g_{\mu\nu}^+ - g_{\mu\nu}^-\right)|_\Sigma \partial_\alpha \Phi \ . \tag{4.61}$$

The last term with the delta distribution must vanish at Σ, because the Christoffel symbols constructed from this metric would otherwise have terms proportional to $\delta(\Phi)\Theta(\Phi)$. Therefore the metric components must be continuous over Σ in the coordinates x^μ. To make this statement coordinate-independent, we can write it in terms of the induced metric

$$h_{ab}^+|_\Sigma - h_{ab}^-|_\Sigma = 0 \ . \tag{4.62}$$

This is the first junction condition.

The second junction condition is more involved. It turns out that the boundary has an energy-momentum tensor

$$T_\Sigma^{\alpha\beta} = \delta(\Phi) S^{ab} e_a^\alpha e_b^\beta \ , \tag{4.63}$$

where S^{ab} is the three-dimensional energy-momentum tensor of the surface, which in turn is related to the extrinsic curvature tensor of the surface. By equating the singular part of the Einstein tensor and the singular part of the energy momentum tensor via the Einstein equation, the surface energy density is [31] (page 88)

$$S_{ab} = -\frac{\epsilon}{8\pi G}\left[K_{ab}^+ - K_{ab}^- + \left(K^+ - K^-\right) h_{ab}\right]_\Sigma \ , \tag{4.64}$$

where the entire expression is evaluated on Σ. Thus in order to avoid the thin shell divergence in (4.63), the extrinsic curvature tensor must be continuous over Σ,

$$K_{ab}^+|_\Sigma - K_{ab}^-|_\Sigma = 0 \ . \tag{4.65}$$

This is the second junction condition. It can be proven that these two conditions are sufficient and necessary for the full four-dimensional Riemann tensor to be non-singular at Σ [119]. The first condition is necessary for the solution to be valid and the second condition keeps it from being singular.

In the case of the LTB metric, the first junction condition imposes that the model-defining functions $M(r)$, $E(r)$ and $t_B(r)$ must be continuous through the surface at some coordinate radius r_b. The second junction condition requires that $R'/|R'|$ is continuous through the surface, that is, R' cannot change sign. Kottler holes can be embedded into a FRW background if the embedding radius r_b is comoving in the FRW coordinates, but expanding in the usual stationary Kottler coordinates.

4.3.2 Distribution of holes

As long as the junction conditions hold, two patches of spacetime can be glued together. In the case of an FRW background and spherically symmetric holes, we can choose the coordinates so that the origin of the FRW model coincides with the origin of the LTB model. In order for the spherically symmetric hole to satisfy the junction conditions throughout the embedding surface, the surface must be spherically symmetric, so it is located at some coordinate radius r_b, which may in general depend on time, but not on the angles. As long as the holes do not overlap, the process can be repeated arbitrarily many times, since the holes do not affect the background solution outside the embedding radius.

There are many ways to fill a box with spheres, and such problems have been studied a lot in mathematics. If the spheres can have varying sizes, a packing similar to the two-dimensional

Apollonian Gasket is possible, which fills the entire volume by filling the empty regions between spheres with ever smaller spheres. For spheres with uniform size, the packing can never be perfect. The packing efficiency is quantified by the *packing fraction*, the volume of the spheres divided by the total volume in the limit where the box is large. A cubic lattice has packing fraction $\pi/6 \simeq 0.52$ and a hexagonal lattice has packing fraction $\frac{\pi}{3\sqrt{3}} \simeq 0.60$. The most efficient lattice is the cubic close packing lattice, with a packing fraction $\frac{\pi}{3\sqrt{2}} \simeq 0.74$.

A random arrangement of holes is typically less efficient than the lattices, although by complicated algorithms, similar packing fractions can be achieved. The simplest way to generate a random arrangement is to pick positions for the hole centres at random, and simply discard any that overlap with an earlier hole. Such a method is easy to implement, but ends up being relatively inefficient if the entire universe is populated with holes. In paper **III**, we considered a total of ~ 250000 holes with a packing fraction of 0.34. For such a large number of holes and packing fraction, this algorithm is fairly inefficient, and it gets worse fast when a larger packing fraction is wanted.

Let us construct an arrangement of holes in a three-dimensional Euclidean space. Let the observer be located in the origin, holes be at locations $\mathbf{x}_i$, and let the direction of the geodesic be $\hat{\mathbf{e}}$. The impact parameter is proportional to

$$c_\phi \propto \sqrt{\mathbf{x}\cdot\mathbf{x} - (\mathbf{x}\cdot\hat{\mathbf{e}})^2} \ , \tag{4.66}$$

and the proportionality constant comes from the requirement that the square root in (4.52) is zero at the correct value of R. To calculate the hole's alignment with respect to the Sachs basis of the beam, we project the beam onto the plane perpendicular to the beam,

$$\mathbf{v}_i = \mathbf{x}_i - (\mathbf{x}_i\cdot\hat{\mathbf{e}})\hat{\mathbf{e}} \ , \tag{4.67}$$

and then compare the phases. We can define the Sachs basis of the first hole to be aligned with the principal axis of shearing, in which case the phase is zero for the first hole. Then

$$\chi_i = \pm\arccos\left(\frac{\mathbf{v}_0\cdot\mathbf{v}_i}{|\mathbf{v}_0||\mathbf{v}_i|}\right) \ . \tag{4.68}$$

In many papers on Swiss Cheese models, the holes have not had a fixed arrangement. Instead, they are dynamically generated along each geodesic separately. The impact parameter c_ϕ has a probability distribution

$$P(c_\phi) = Nc_\phi \ , \tag{4.69}$$

N being a normalisation constant. This reflects the fact that the probability of passing through a shell is proportional to its distance from the hole's centre. The alignment of the hole with respect to the Sachs basis is random with an uniform distribution. Finally, the distance between two voids is a random variable with some distribution that depends on the distribution of holes. The packing fraction of the distribution can be difficult to find in such cases.

Chapter 5

Optics in a clumpy universe

The aim of this chapter is to form a synthesis of the themes discussed in the earlier chapters, and to describe the research done in papers **I**, **II** and **III**. The chapter starts with models that have only one large void, and in particular the Cold Spot, which was the topic of paper **II**. Then it moves to models with more complicated distributions of matter, focusing mostly on Swiss Cheese models. The Swiss Cheese models are considered in terms of large modification of the distance-redshift relation, as was done in **I**, and in terms of weak lensing, as was done in **III**.

5.1 Single void: The case of the Cold Spot

Light propagation through a single void has been studied for example using the LTB metric [120, 121, 122, 123, 124] and second order perturbation theory [125, 126], in the context of calculating the change in redshift, and thus the observed CMB temperature. In these studies, the observer is typically well outside the void, as being inside would only generate monopole and dipole-type terms, which are not used in the usual CMB analysis.

Another line of research has been towards what would happen if the observer was located inside one massive void. In these cases, the observer is typically located in the centre of the void, so the main contribution to the temperature is a monopole term. Instead, people have considered such models to change the observed distance-redshift relation. It has been shown that an LTB void could produce any distance-redshift relation if the parameters are chosen correctly [127]. Large voids have been attempted to use to explain dark energy [11, 128, 129, 130] but such models are strongly constrained by including complementary data sets [131, 132, 133, 134, 135, 136].

5.1.1 The Cold Spot

The usual CMB analysis decomposes the temperature anisotropies into multipoles that are independent of angle. To look for local anomalies, methodology that does not mix the information from all locations is needed. One possibility is using wavelets, a kind of localised Fourier transformation. A particular realisation of a wavelet is the Spherical Mexican Hat Wavelet (SMHW), which was proposed as a probe of local non-Gaussianities in the CMB by Cayón et al. [137]. Examples of the SMHW smoothing function for different smoothing scales are shown in Figure 5.2.

In [138], Vielva et al. reported on a non-Gaussian feature seen in the WMAP satellite one year maps using the SMHW method. The feature is a large cold region centred at ($\theta = -147°$, $\phi = 209°$) with a diameter of about $\sim 10°$ and a central temperature fluctuation of $\Delta T \sim -150\mu$K. The Cold Spot is shown in Figure 5.1, both before and after applying the wavelet transformation on the map. The result has been verified by multiple groups, using different

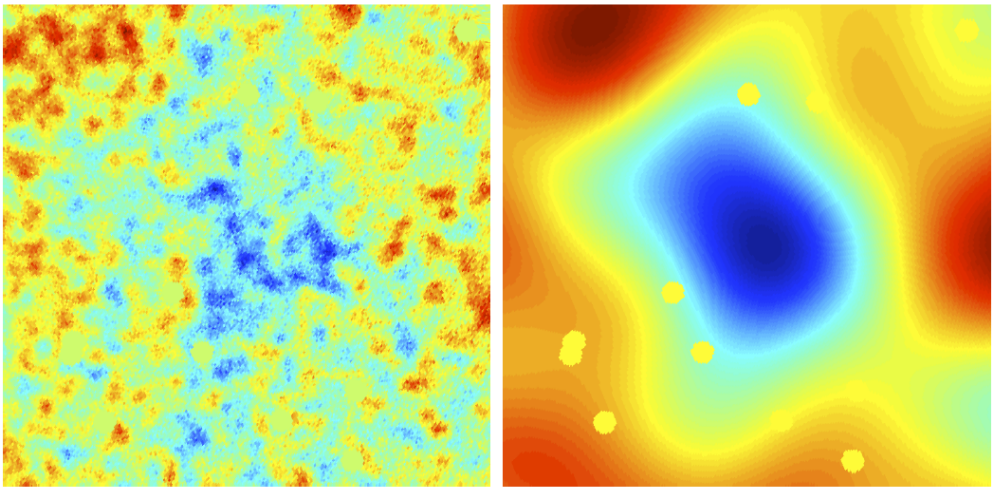

Figure 5.1: The Cold Spot in the CMB map (*left*) and the same region smoothed using wavelets (*right*). The yellow spots are masked foreground objects. Figure from [84].

WMAP and Planck satellite maps, and the anomaly seems to persist at about 3σ significance, although the interpretation of such a number is complex (see [139] for the analysis).

Many explanations have been proposed for the Cold Spot. Foreground effects and the Sunyayev-Zel'dovich effect can not give a large contribution to the Cold Spot [84] as the frequency dependence around the Cold Spot is not anomalous. A systematic cause is possible in principle, but since both WMAP and Planck agree on the signal separately, it seems unlikely at this point. Cosmic textures have also been proposed as a potential cause for the Cold Spot [140]. Finally, as we have seen in the earlier chapters, a large void can generate temperature fluctuations in the CMB via the ISW and higher order effects. If the void is large enough, it could well generate such a large temperature fluctuation [125, 126]. If a smaller void would accidentally happen to align with a primordial Cold Spot, that could also contribute to the signal [141].

5.1.2 Detection of a void at the direction of the Cold Spot

A large void was detected in the direction of the Cold Spot by Szapudi et al. [142] and in a companion paper it was claimed that this void was sufficiently large and deep to produce the Cold Spot [143]. The void fits the density profile

$$\delta(r) = -\delta_0 \left(1 - \frac{2r^2}{3r_0^2}\right) \exp(-r^2/r_0^2) \ , \tag{5.1}$$

with the density contrast at void centre today $\delta_0 = 0.25$ and the decay length $r_0 = 195h^{-1}$ Mpc if the void is centred at redshift $z_c = 0.155$. For a flat ΛCDM universe with $\Omega_\Lambda = 0.7$, this redshift corresponds to a comoving distance of $D_c = 448h^{-1}$ Mpc $= 2.3r_0$, so the observer is located in the tail of the outer overdense shell. The claim that such a void could explain the entire Cold Spot was unexpected for several reasons. For example, the detected void is not terribly rare. Based on the peak model of structure formation, one can estimate that in the local universe there should be approximately 20 voids that are equally extreme as this one [2]. The question then arises: if the Cold Spot is caused by such a void, why is there only one such spot on the CMB map? Also, the void is not deep, with its density contrast in the centre being only $\delta_0 = -0.25$. The expectation is that linear perturbation theory would hold reasonably well

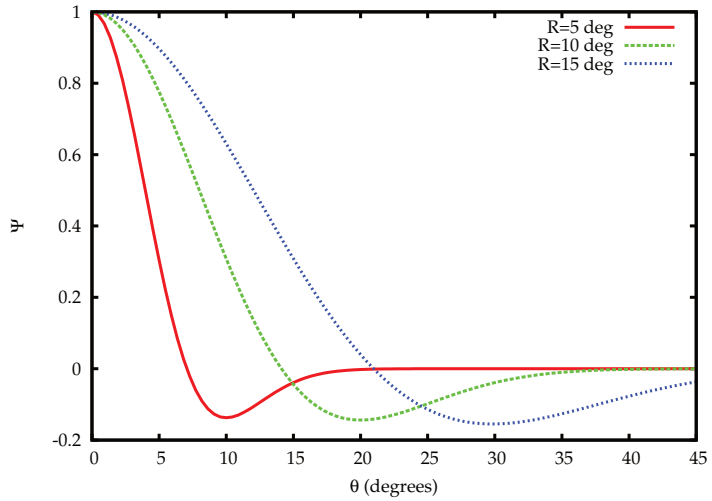

Figure 5.2: The Spherical Mexican Hat Wavelet smoothing functions as a function of the angular separation θ for smoothing scales R corresponding to 5°, 10° and 15°. The amplitude has been normalised to one at $\theta = 0°$.

for structures like this, so why is the temperature signal and order of magnitude greater than the first order perturbation theory estimation, $\Delta T \sim -20\mu$K?

The authors of [143] claimed that although the linear ISW effect is small, the second order RS effect is an order of magnitude larger. They backed this up by presenting a calculation done using an LTB model with density profile (5.1) and finding a temperature profile that roughly matches the Cold Spot. Such a massive breakdown of perturbation theory would provide compelling evidence that perturbation theory cannot be reliably used to model light propagation in large cosmic structures.

We investigated the claim in [2] and found that the LTB void with density profile (5.1) does indeed produce a temperature fluctuation of $\sim -100\mu$K at the centre. However, most of the signal comes from a dipole, i.e. one side of the sky being colder than the other. Thus the temperature profile of such a void is very different from the profile of the Cold Spot. The dipole is caused by the fact that the observer is still within the overdense tail of the density profile. We got the same result using second order perturbation theory, where the dipole term dominates, the ISW term accounts for the expected $\sim -20\mu$K and the RS term is negligible [2]. Such a feature would not show in the usual CMB analysis, as the dipole is typically removed before looking at the higher multipoles. Note that the authors of [143] updated their analysis for the newest version of their paper. Their updated calculations agree with ours, although their conclusion still is that the void is somehow causally linked to the Cold Spot.

Finally, it is worth pointing out that the Cold Spot is not anomalous due to its central coldness. Looking at simulated CMB maps and finding their coldest spots using the same algorithm as with the real CMB sky, the central temperature is well within the expected range of values. In Figure 5.3, the temperature profile of the Cold Spot is compared to the range of profiles calculated from simulated maps. It is clear that nowhere does the Cold Spot profile cross the 2σ contour. Instead, the Cold Spot appears anomalous in the analysis because the colder than average central region is surrounded by a hotter than average ring. Due to their shape, the wavelet basis functions pick up the central cold region and outer hot region with opposite signs, leading to an amplified result.

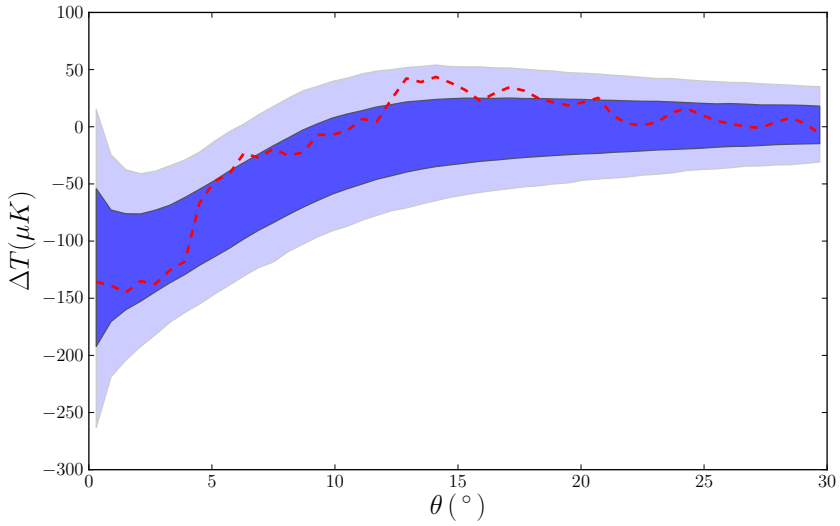

Figure 5.3: Temperature profile of the Cold Spot from Planck SMICA map (red dashed line) compared to the 68% and 95% confidence ranges for the temperature profile of the coldest spot in 10000 random Gaussian maps using ΛCDM parameters. Figure from [2].

5.1.3 Is it anomalous?

It is at least partially a matter of taste whether the Cold Spot should be considered anomalous or not. We are animals that see patterns wherever we look, such as seeing the initials of Stephen Hawking in the WMAP 7 year CMB map [144]. Although the occurrence of such a feature in a random map is extremely small, it would be silly to start looking for 'explanations' for this anomaly. The reason is that there is no reason to look for anyone's initials in the CMB. The initials were spotted *a posteriori*, which makes their significance appear higher than it actually is. In a dataset as rich as the CMB temperature sky, there will always be some anomalous structures and signals. The case of the Cold Spot is not so clear cut, as there is a sensible case *a priori* for looking for anomalies using a compensated spherical filter. Nonetheless, the probabilities and sigma values associated with such anomalies should probably be taken with a large grain of salt.

However, there is also the matter of the detected void. It seems like an unlikely coincidence that a relatively rare void would be seen precisely where the Cold Spot lies, if it does not significantly contribute to the Cold Spot's anomalousness. Although the conclusion is that such a void cannot generate the Cold Spot on its own, it does call for further analysis as it definitely contributes partially to it. In [141], before the detection of the void in [142], Inoue found that the best fit for the Cold Spot was that 90% of its temperature signal came from the last scattering surface and 10% from a void with radius $\sim 600h^{-1}$ Mpc and density contrast $\delta \sim 0.01$ at redshift $z \sim 1$. Thus it is larger, less underdense and further away than the void discovered by Szapudi *et al.* A careful analysis of the combined effect of the void detected by Szapudi *et al.* and a fluctuation at the last scattering surface has not been done at this time. However, such a result cannot resolve the anomalousness of the Cold Spot in any case, as the alignment of a void with an already cold region is also quite an unlikely accident.

5.2 The distance-redshift relation in Swiss Cheese

Swiss Cheese models have often been used to study the distance-redshift relation (e.g. [145, 146, 147, 148, 149, 150, 151, 152, 153, 154, 155, 110, 156]), and in some cases large differences in the

relation have been claimed, compared to the distance-redshift relation of a corresponding FRW model. There are two possible ways in which inhomogeneities could influence the relation. One possibility is if they bias the sampling of geodesics that the observer sees, the other is if the model has a non-negligible backreaction component.

5.2.1 Backreaction

Shell crossings and junction conditions limit the class of possible solutions that can be joined together into a Swiss Cheese. In the article **I** we attempted to find ways to construct Swiss Cheese models that have a non-negligible backreaction component. We proved the following theorem.

Theorem. Assuming that conditions $(1-5)$ are satisfied, the average expansion rate of a Swiss Cheese spacetime with no cosmological constant and with Szekeres holes is close to that of the background.

1. The centre of the hole is regular, $R(0,t) = 0$ for all t;
2. The metric function R is monotonic;
3. There is a big bang singularity at time $t_B(r)$ and the spacetime is nearly equally old everywhere, $t_0 - t_B(r) \simeq t_0$ for all r, where t_0 is the time today;
4. The Szekeres solution matches to an FRW background at a comoving radius r_b;
5. Today the holes are small compared to the curvature radius of the universe.

It is straightforward to show that the conditions imply that $|E| \ll 1$ and that this in turn implies that the expansion rates must be close to each other [1]. Physically the proof is very intuitive. The metric must be continuous through the embedding surface, so the outer edge of the hole must always expand at the same rate as the background. If the centre of the hole is regular, then any deviation to the expansion rate must come from the extra curvature term in the volume element (4.26). However, if a shell at coordinate radius r has $E(r) > 0$, then $E(r)$ must be small or else the shell will collide with the boundary. If another shell has $E(r) < 0$, then $|E(r)|$ must be small, or otherwise the shell will collapse in a time smaller than the age of the universe.

The universe is nearly homogeneous at large scales and at early times, so the holes cannot today be the same size as the cosmic horizon, nor can the bang time function vary drastically, so it is difficult to see how assumptions 3 and 5 could be violated in the real universe. Assumptions 1 and 4 are less strongly motivated, and they exclude for example Schwarzschild holes from the domain of this proof. Finally, this formulation of the proof only works for models where the cosmological constant vanishes. It seems possible that a similar theorem could be proven for the general case with a non-vanishing cosmological constant, but making it rigorous is not as easy.

We investigated the breakdown of assumption 2 in [1], and attempted to construct a Swiss Cheese model where the backreaction term would be large. The function R can be chosen so that in some region inside the hole, $R(t,r) > R(t,r_b)$. If R' has two zeroes at r_1 and r_2, the model can be understood as three different LTB solutions joined together. One model with $R' \geq 0$ in the range $0 \leq r < r_1$, second with $R' \leq 0$ in the range $r_1 \leq r < r_2$ and third with $R' \geq 0$ and $r_2 \leq r \leq r_b$. At r_1 and r_2 there are discontinuities in the extrinsic curvature tensor, which induce thin singular shells at these locations. If the functions $M(r)$, $E(r)$ and $t_B(r)$ are chosen so that $M'(r_i) = E'(r_i) = t_B'(r_i) = 0$, the thin shells remain stationary at r_i and there are no shell crossings in the model. Furthermore, the model can be constructed so that these singular shells do not affect the average expansion rate by keeping $H_\parallel = \dot{R}'/R'$ finite at r_i. The

expansion rate may have a local discontinuity at the shell locations, but as the shells have have zero measure, the total contribution from the shells to the volume averages vanishes.

In the model studied in [1], $\mathcal{Q}_\mathcal{D}$ is not negligibly small, but its contribution accounts for $\sim 1\%$ of the average expansion rate in (2.72). Thus it is too small to contribute noticeably to the explanation of the apparent accelerated expansion. Even though $\mathcal{Q}_\mathcal{D}$ is small, the holes and the background expand very differently, and this difference can be made arbitrarily large as the model can be constructed so that there are no shell crossings. It should be also noted that if the real universe would have an equally large backreaction term, that would induce a significant error into the estimation of cosmological parameters. However, in realistic Swiss Cheese models with only dust, backreaction is expected to be much smaller based on our proof.

5.2.2 Biased sampling

Biased sampling occurs when the geodesics that pass through observer's location sample the universe unevenly. There are two distinct possibilities here. First, this may be the property of the geodesics themselves. Second, it may be that the bias occurs because only a subset of all geodesics is considered. The first is arguably more interesting, whereas the second is more mundane, but also the one that appears to occur most often in numerical analyses. The second category also includes situations where the geodesics are weighed improperly.

There is a famous argument by Weinberg [157], further elaborated by Kibble and Lieu [158], arguing that although small transparent clumps of matter can change the distance-redshift relation for a single geodesic, the average distance over a surface of constant redshift must be almost independent of the clumps, as the total flux of photons through the surface cannot change. The 'almost' is there because the total photon flux over the surface is conserved, but luminosity distance is not linear in the flux. There are some examples of scenarios where the Weinberg argument manifestly breaks down, such as models where the null geodesics form caustics [159]. Furthermore, the argument assumes that the surface area of the surface of constant redshift is unaffected by lensing, which is precisely what the proof is attempting to show. It has been argued however, that at least in perturbation theory, the change in the area is negligible [160].

If the Weinberg argument holds, then the inverse magnification should average to one over angles,

$$\langle \mu^{-1} \rangle_\Omega = 1 \ , \tag{5.2}$$

and the average shift in distance anisotropies should be proportional to the variance of distance for a single beam squared [160, 3], and so it should be small. Using (3.53) and (3.54),

$$\langle \Delta D_A / \bar{D}_A \rangle_\Omega = -\frac{1}{2} \langle \Delta D_A^2 / \bar{D}_A^2 \rangle_\Omega \ . \tag{5.3}$$

The distance shift averaged over angles should be negative, regardless of the properties of the lenses, and it should be small compared to the variance of a single geodesic. Instead of the angles, one can also average over the area of a constant-redshift surface, in which case the Weinberg argument gives

$$\langle \mu \rangle_A = 1 \ , \tag{5.4}$$

and

$$\langle \Delta D_A / \bar{D}_A \rangle_A = \frac{3}{2} \langle \Delta D_A^2 / \bar{D}_A^2 \rangle_A \ . \tag{5.5}$$

If the Weinberg argument holds, then there cannot be any intrinsic bias on the level of the geodesic equations. Rather, the bias must be imposed by hand when considering the sampling of the light cone.

Despite the Weinberg argument, some earlier papers have suggested that Swiss Cheese models could influence the distance-redshift relation in a considerable way. It seems that all of these

results are large due to some kind of bias in the way the null geodesics have been chosen [3]. The original example is the paper by Marra, Kolb, Matarrese and Riotto (MKMR) [147], where the authors study light propagation through five aligned voids. The voids were perfectly aligned, each acting to de-magnify the image, making the object behind them appear to be further away. The MKMR distance-redshift relation through the voids was close to the FRW relation of a universe with $\Omega_m = 0.6$ and $\Omega_\Lambda = 0.4$, even though the model had no cosmological constant. The MKMR result was investigated by multiple groups [161, 150] and it was found that the demagnification reduces by orders of magnitude if the voids are not perfectly aligned, but instead the impact parameters are randomised appropriately. A more subtle example of improper sampling was present in the first version of [150], where Szybka generated the matter distribution dynamically using an uniform probability distribution for the impact parameter c_ϕ instead of (4.69), leading to a larger shift in distance, since the volume of the void centres was sampled proportionally too often.

A more physically motivated example is given by Fleury et al., who have studied a Swiss Cheese model with Kottler holes [154, 155, 110]. They consider only geodesics that pass the black holes at a distance that is much greater than the hole's Schwarzschild radius, leading to an incomplete sampling of the full spatial volume. They argue that this is natural if matter is concentrated into opaque clumps. Even if light rays could pass close to the Schwarzschild radius, such paths are relatively rare, so they would only show up in the very tail of the distribution. Their results follow closely the famous Dyer-Roeder distance formula [16, 17, 162, 163, 164], leading to a large shift in the distance-redshift relation if a large fraction of the volume is taken by holes. The value of the cosmological constant affects their results considerably. A smaller cosmological constant leads to a larger shift and vice versa.

Finally, most Swiss Cheese models consider the observer and the source to be located in the background. Although this is a natural choice when not interested in the boundary terms, this can in principle give a non-zero bias when comparing to a calculation where the observer and source are located completely randomly.

5.3 Weak lensing in Swiss Cheese

The usual first order weak lensing results have been extended to include more effects. Bonvin et al. calculated the luminosity distance in first order perturbation theory using the covariant formalism of Section 3.4 [165]. The effect of peculiar velocities are discussed in [166]. Second order weak lensing formalism is developed in [167, 168]. There was also a claim by Clarkson et al. that second order lensing could produce a $\sim 1\%$ systematic shift in the distance to the CMB [169]. However, a more careful analysis revealed that the effect is much smaller [170, 171, 160], and the large result was again due to the incorrect weighing of the null geodesics.

Another way to extend the usual weak lensing analysis is to use an exact Swiss Cheese model. In this case, comparison to the results of perturbation theory is difficult, as the matter power spectra of the two models are difficult to match perfectly. Nonetheless, one can calculate the convergence κ and shear γ in a Swiss Cheese model using the covariant formalism and then relating the covariant quantities to weak lensing quantities via (3.53) and (3.54). As long as these quantities are small, the comparison is straightforward [151, 3].

We investigated a Swiss Cheese model with a fully randomised distribution of holes in paper [3]. Based on the points raised in the previous section, we expected the shift in distance and redshift to be small, so our idea was to remove most of the potential biasing factors from the analysis. The aim was to see if there are any interesting effects left. We considered a fixed, randomly distributed arrangement of holes, populating the universe all the way up to redshift of $z \sim 6$. This value of redshift was chosen for two reasons. First, we wanted to calculate the distance to the CMB last scattering surface. The lensing signal should be maximal for a lens

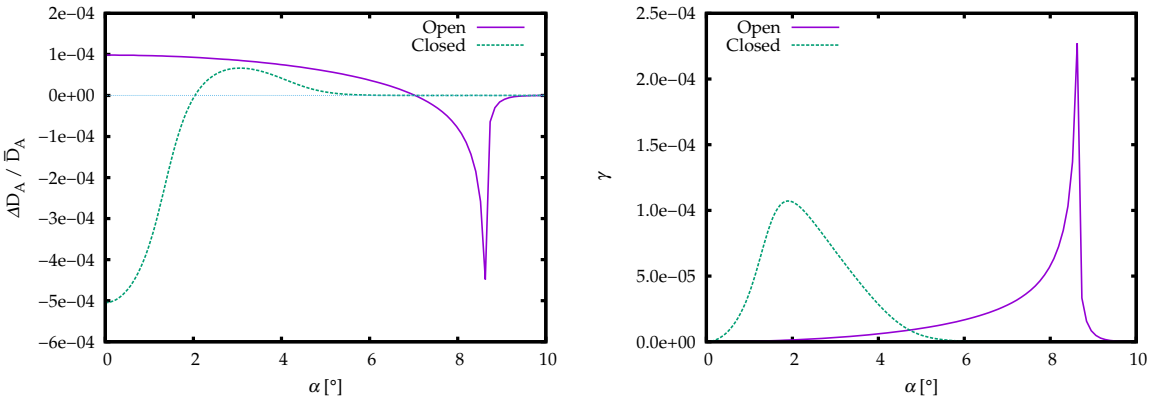

Figure 5.4: Angular profiles for the change in angular diameter distance compared to the background and integrated null shear for a single hole in the Swiss Cheese model [3]. The centre of the hole is $200h^{-1}$ Mpc away from the observer, and α is the angle from the hole centre as seen on the sky.

that is approximately halfway between the observer and the source, and $z = 6$ is beyond the halfway point. Therefore we have included the holes that produce most of the signal. Second, holes that have comoving radius today of $50h^{-1}$ Mpc have such a small angular size beyond this redshift that we cannot resolve any of the details of the distribution. We considered two different LTB profiles. The "open" model has $E \geq 0$, so it has an underdense centre and an overdense outer shell. The "closed" model has $E \leq 0$, with an overdense centre and an underdense outer shell. The two profiles have distinctly different profiles for $\Delta D_A/\bar{D}_A$ and γ, plotted in Figure 5.4. In particular note that the distance and the shear both have sharp peaks in the open model, whereas the curves are smoother in the closed model.

We calculated the sky maps for redshift, distance and shear with resolution $12288 = 12 \times 32^2$ evenly spaced pixels using the HEALPix routines [172]. We also calculated the power spectra for these quantities, although the resolution is not good enough to see any structure in the power spectra of distance or shear. This is in contrast to a similar calculation by Valkenburg [173], who found very striking correlation patterns even for large scales. The difference arises because Valkenburg used a cubic lattice arrangement for the holes, leading to large correlations between different holes, whereas in our arrangement the correlations are negligible. The real universe lies somewhere between these two extremes.

We used the bootstrapping algorithm to produce new sky maps from the original map to study the variance of statistical quantities. In particular we were interested whether the systematic shift in the distance, $\langle \Delta D_A/\bar{D}_A \rangle_\Omega$ was statistically significant. The probability density function for this quantity is plotted in Figure 5.5. The closed model mean does not deviate from zero, but in the open model, the mean is different from zero at about 2σ confidence.

If the area of a constant-redshift surface remains unchanged by the matter distribution, then the equation (5.3) should hold. In our open model however, the quantity $\langle \Delta D_A/\bar{D}_A \rangle_\Omega$ was smaller than $-\frac{1}{2}\langle \Delta D_A^2/\bar{D}_A^2 \rangle_\Omega$ only in 1.4% of the bootstrap maps. On the other hand, the results for the closed model are completely compatible with the Weinberg argument. Note that the error limits are calculated assuming that each pixel is an independent random variable, which is of course not exactly true, as the pixels near each other can be strongly correlated. However, it seems unlikely that including the correlation would change the error estimate so drastically that it would affect our conclusions. The assumption that each pixel is independent means that the standard deviation in the mean of N pixels σ_N and the standard deviation of

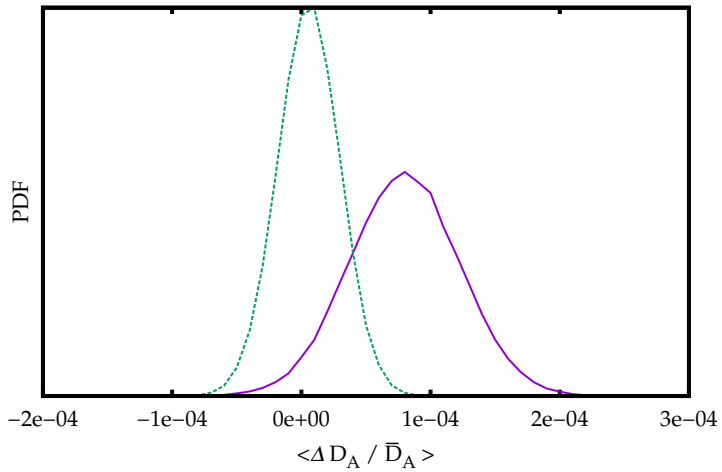

Figure 5.5: The probability density function for $\langle \Delta D_A / \bar{D}_A \rangle_\Omega$ calculated using the bootstrapping algorithm. The y-axis is left un-normalised.

one pixel σ_1 are related via

$$\sigma_N = \frac{\sigma_1}{\sqrt{N}} \ . \tag{5.6}$$

This relation can be used to estimate the required number of pixels for a significant detection, assuming that the estimate from our results is correct.

Our results seem to indicate that the area of the constant-redshift surface around the observer may be altered by the matter distribution, although the statistical significance is not high enough to make a solid claim. However, there are other possible explanations for the result as well, that would need to be taken into account more thoroughly to get a reliable answer. One potential problem is that we have generated the error estimates only using a single realisation of the ensemble of possible sky maps. Since we only have a relatively small number of pixels, it is possible that we are missing some effects that occur rarely for a single geodesic, but which nonetheless produce a large effect on the average. In particular, the distance profile of a hole in the open model has a very sharp peak near the edge of the hole, which can be seen from Figure 5.4. On the other hand, the closed model has a smoother profile. It may be that the sharp peak is not probed sufficiently well in our setup, and this can cause the average quantities to be evaluated inadequately. Running the same calculation with a better resolution would probably help to resolve this issue. Unfortunately, the computation takes quite a lot of time per pixel, so a calculation with higher resolution would require more work and probably also a supercomputer.

Nonetheless, our results underline the importance of doing proper statistical analysis when trying to find deviations from the background. Especially for the distance, the mean shift is always expected to be much smaller than the variance of a single beam. To get a statistically significant number out, a large number of samples is needed. In addition, one must be very careful when weighing geodesics and taking averages, as this can lead to unintended biases in the results. Swiss Cheese models have often been studied in an attempt to find large deviations in the distance compared to that of the background. However, the result does not have to be large in order to be interesting. Any rigorous and statistically significant result with proper geodesic averaging that breaks the Weinberg argument would expose a real need to re-consider the underlying assumptions of the concordance model. This may be the most interesting future application of the Szekeres Swiss Cheese models in cosmology.

Chapter 6

Discussion

The concordance model of cosmology relies on the assumption that on cosmological time and length scales, the universe can be described using a perturbed FRW metric. This assumption has been shown to be true in special cases, and no clear signal of its breakdown has been seen from the data, although some hints with a low statistical significance, such as the Cold Spot and the discrepancy in the CMB lensing amplitude have been detected. These anomalies may turn out to be signals of new physics, but at this time they remain mainly curiosities, small blips in otherwise perfect matching of observation and model. Yet the absence of evidence is not evidence of absence. Just because the concordance model is able to fit all the data, it does not follow that it must be true.

My aim in this thesis has been to study exact inhomogeneous cosmological models, and to see if their predictions for observables are significantly different from the predictions of perturbation theory. Many authors have proposed models that appear to produce results that differ noticeably from what is predicted by the concordance model, and I have attempted to understand better these claims. Along with my collaborators, I have studied Swiss Cheese models in detail, attempting to pinpoint the ways in which they can produce such large differences compared to the concordance model. Additionally we examined a claim that was made about a recently discovered supervoid, which was said to be solely responsible for the Cold Spot.

We attempted to find conditions that allow (or disallow) Swiss Cheese models to have a backreaction term that influences the evolution noticeably on large scales. It seems that backreaction must always be small in physically motivated models, although we only managed to prove this partially. This result is due to the way that Swiss Cheese models are constructed – in particular it is due to the fact that the Szekeres solution has no rotation and no pressure, so nothing can counteract the gravitational collapse in these models. Models that expand at a different rate from the background always contain shell crossing singularities when considering cosmologically relevant time scales.

We were the first to study the weak lensing of the CMB in full in Swiss Cheese models, by calculating both the distance perturbation and the integrated null shear. Unfortunately solving the geodesics in the Swiss Cheese model is too time-consuming to probe the small-scale correlations in their entirety. We calculated the sky maps of 12288 pixels for $\Delta T/\bar{T}$, $\Delta D_A/\bar{D}_A$ and γ. From these we calculated the power spectra up to the multipole $l = 96$, which is not enough to see all of the structure in them. Nonetheless we argued that the overall power in small scales should not be too much larger than in the scales we looked at. Our results for the systematic shift in distance were at odds with the Weinberg argument, with a probability of 1.4%. A more careful study, with more pixels and better analysis of potential systematic problems would be needed to see if this was just a fluke, or whether the area of a constant-redshift surface is really changed in our model.

In our attempts to find deviations from the concordance model, we found that in most cases

it held up very well. For voids in general, we found no signs of the breakdown of perturbation theory, even for highly nonlinear voids, such as the comparison model in [2]. For Swiss Cheese models, it seems that the only way to get results that differ greatly from the concordance model is to consider opaque matter clumps, which leads to the well known Dyer-Roeder distance-redshift relation. Other attempts lead to either entirely unphysical models, as the Tardis model in [1], or nearly identical results to the concordance model, such as in [3].

For the future it seems that there are two diverging paths. One is trying to construct models that take effects of pressure and rotation better into account, so they describe the non-linear growth of structures more accurately. It is possible that such models could contain a large backreaction component, which would alter their time-evolution from the concordance model. Another one is studying Swiss Cheese models in increasing detail, improving the resolution and accuracy of the calculation to hone in on the prediction of the Weinberg argument. It would be a very interesting finding to see that the Weinberg argument can be broken by simple non-linear structures, even if the difference is small. It would serve as a proof of concept that small-scale structure can influence the area of the constant-redshift surface, and thus make it important to re-consider the importance of this effect in the real universe.

Appendix A

Christoffel symbols and curvature tensor of the LTB metric

A.1 Christoffel symbols

The Christoffel symbols for the LTB metric are

$$\Gamma^t_{rr} = X\dot{X} \qquad \Gamma^t_{\theta\theta} = R\dot{R} \qquad \Gamma^t_{\phi\phi} = R\dot{R}\sin^2\theta \tag{A.1}$$

$$\Gamma^r_{rr} = \frac{X'}{X} \qquad \Gamma^r_{tr} = \frac{\dot{X}}{X} \qquad \Gamma^r_{\theta\theta} = -\frac{RR'}{X^2} \qquad \Gamma^r_{\phi\phi} = -\frac{RR'}{X^2}\sin^2\theta \tag{A.2}$$

$$\Gamma^\theta_{t\theta} = \frac{\dot{R}}{R} \qquad \Gamma^\theta_{r\theta} = \frac{R'}{R} \qquad \Gamma^\theta_{\phi\phi} = -\sin\theta\cos\theta \tag{A.3}$$

$$\Gamma^\phi_{t\phi} = \frac{\dot{R}}{R} \qquad \Gamma^\phi_{r\phi} = \frac{R'}{R} \qquad \Gamma^\phi_{\theta\phi} = -\cot\theta\ . \tag{A.4}$$

A.2 Riemann tensor

The components of the Riemann tensor are

$$R_{trtr} = -X\ddot{X} \qquad R_{t\theta t\theta} = -R\ddot{R} \qquad R_{t\phi t\phi} = -R\ddot{R}\sin^2\theta \tag{A.5}$$

$$R_{t\theta r\theta} = -R\dot{R}' + \frac{\dot{X}}{X}RR' \qquad R_{t\phi r\phi} = \sin^2\theta R_{t\theta r\theta} \tag{A.6}$$

$$R_{r\theta r\theta} = -RR'' + R\dot{R}X\dot{X} + RR'\frac{X'}{X} \qquad R_{r\phi r\phi} = \sin^2\theta R_{r\theta r\theta} \tag{A.7}$$

$$R_{\theta\phi\theta\phi} = R^2\sin^2\theta\left(1 + \dot{R}^2 - \frac{R'^2}{X^2}\right)\ . \tag{A.8}$$

A.3 Ricci tensor

The components of the Ricci tensor are

$$R_{tt} = \frac{\ddot{X}}{X} + \frac{2\ddot{R}}{R} \tag{A.9}$$

$$R_{tr} = \frac{2\dot{R}'}{R} - \frac{R'\dot{X}}{RX} \tag{A.10}$$

$$R_{rr} = -X\ddot{X} + \frac{2R''}{R} - 2X\dot{X}\frac{\dot{R}}{R} - \frac{2R'X'}{RX} \tag{A.11}$$

$$R_{\theta\theta} = \frac{RR''}{X^2} - R\ddot{R} - \frac{RR'X'}{X^3} - R\dot{R}\frac{\dot{X}}{X} - (1+\dot{R}^2) + \frac{R'^2}{X^2} \tag{A.12}$$

$$R_{\phi\phi} = \sin^2\theta R_{\theta\theta} \ . \tag{A.13}$$

A.4 Ricci scalar

The Ricci scalar is

$$R = -2\left(\frac{\ddot{X}}{X} + \frac{2\ddot{R}}{R} + \frac{2\dot{R}\dot{X}}{RX} - \frac{2R''}{RX^2} + \frac{2R'X'}{RX^3} + \frac{1+\dot{R}^2}{R^2} - \frac{R'^2}{R^2X^2}\right) \ . \tag{A.14}$$

A.5 Weyl tensor

The Weyl tensor has only one independent degree of freedom

$$W \equiv \frac{\ddot{X}}{X} + \frac{R''}{RX^2} - \frac{\dot{R}\dot{X}}{RX} - \frac{R'X'}{RX^3} - \frac{\ddot{R}}{R} + \frac{1+\dot{R}^2}{R^2} - \frac{R'^2}{R^2X^2} \ . \tag{A.15}$$

The components of the Weyl tensor are

$$C_{trtr} = -\frac{X^2}{3}W \qquad C_{t\theta t\theta} = \frac{R^2}{6}W \tag{A.16}$$

$$C_{t\phi t\phi} = \frac{R^2}{6}\sin^2\theta W \qquad C_{r\theta r\theta} = -\frac{R^2X^2}{6}W \tag{A.17}$$

$$C_{r\phi r\phi} = -\frac{R^2X^2}{6}\sin^2\theta W \qquad C_{\theta\phi\theta\phi} = \frac{R^4}{3}\sin^2\theta W \ . \tag{A.18}$$

A.6 Einstein tensor

The components of the Einstein tensor are

$$G_{tr} = \frac{2\dot{R}'}{R} - \frac{2R'\dot{X}}{RX} \tag{A.19}$$

$$G_{tt} = \frac{-2\dot{R}\dot{X}}{RX} + \frac{R'^2}{R^2X^2} - \frac{1+\dot{R}^2}{R^2} + \frac{2R''}{RX^2} - \frac{2R'X'}{RX^3} \tag{A.20}$$

$$G_{rr} = X^2\left(\frac{2\ddot{R}}{R} + \frac{1+\dot{R}^2}{R^2} - \frac{R'^2}{R^2X^2}\right) \tag{A.21}$$

$$G_{\theta\theta} = R^2\left(\frac{\ddot{R}}{R} - \frac{R''}{RX^2} + \frac{R'X'}{RX^3} + \frac{\dot{R}\dot{X}}{RX} + \frac{\ddot{X}}{X}\right) \tag{A.22}$$

$$G_{\phi\phi} = \sin^2\theta G_{\theta\theta} \ . \tag{A.23}$$

Bibliography

[1] M. Lavinto, S. Räsänen, and S. J. Szybka, *Average expansion rate and light propagation in a cosmological Tardis spacetime*, *JCAP* **12** (Dec., 2013) 51, [arXiv:1308.6731].

[2] S. Nadathur, M. Lavinto, S. Hotchkiss, and S. Räsänen, *Can a supervoid explain the Cold Spot?*, *Phys.Rev.* **D90** (2014), no. 10 103510, [arXiv:1408.4720].

[3] M. Lavinto and S. Räsänen, *CMB seen through random Swiss Cheese*, *JCAP* **10** (Oct., 2015) 57, [arXiv:1507.06590].

[4] A. Sandage, *The Change of Redshift and Apparent Luminosity of Galaxies due to the Deceleration of Selected Expanding Universes.*, *ApJ* **136** (Sept., 1962) 319.

[5] A. R. Liddle, *An Introduction to cosmological inflation*, in *High energy physics and cosmology. Proceedings, Summer School, Trieste, Italy, June 29-July 17, 1998*, pp. 260–295, 1999. astro-ph/9901124.

[6] M. Scrimgeour et al., *The WiggleZ Dark Energy Survey: the transition to large-scale cosmic homogeneity*, *Mon. Not. Roy. Astron. Soc.* **425** (2012) 116–134, [arXiv:1205.6812].

[7] S. Nadathur, *Seeing patterns in noise: Gigaparsec-scale 'structures' that do not violate homogeneity*, *Mon. Not. Roy. Astron. Soc.* **434** (2013) 398–406, [arXiv:1306.1700].

[8] **Supernova Search Team** Collaboration, A. G. Riess et al., *Observational evidence from supernovae for an accelerating universe and a cosmological constant*, *Astron. J.* **116** (1998) 1009–1038, [astro-ph/9805201].

[9] **Supernova Cosmology Project** Collaboration, S. Perlmutter et al., *Measurements of Omega and Lambda from 42 high redshift supernovae*, *Astrophys. J.* **517** (1999) 565–586, [astro-ph/9812133].

[10] S. M. Carroll, W. H. Press, and E. L. Turner, *The cosmological constant*, *ARAA* **30** (1992) 499–542.

[11] M.-N. Célérier, *Do we really see a cosmological constant in the supernovae data?*, *A&A* **353** (Jan., 2000) 63–71, [astro-ph/9907206].

[12] C. Wetterich, *Can structure formation influence the cosmological evolution?*, *Phys. Rev.* **D67** (2003) 043513, [astro-ph/0111166].

[13] D. J. Schwarz, *Accelerated expansion without dark energy*, in *18th IAP Colloquium on the Nature of Dark Energy: Observational and Theoretical Results on the Accelerating Universe Paris, France, July 1-5, 2002*, 2002. astro-ph/0209584.

[14] Y. B. Zel'dovich, *Observations in a Universe Homogeneous in the Mean*, *Soviet Astronomy* **8** (Aug., 1964) 13.

[15] J. Kristian and R. K. Sachs, *Observations in cosmology*, *Astrophys.J.* **143** (1966) 379–399.

[16] B. Bertotti, *The Luminosity of Distant Galaxies*, *Royal Society of London Proceedings Series A* **294** (1966) 195–207.

[17] J. E. Gunn, *On the Propagation of Light in Inhomogeneous Cosmologies. I. Mean Effects*, *ApJ* **150** (1967) 737.

[18] M. F. Shirokov and I. Z. Fisher, *Isotropic Space with Discrete Gravitational-Field Sources. On the Theory of a Nonhomogeneous Isotropic Universe*, *Astronomicheskii Zhurnal* **6** (Apr., 1963) 699.

[19] R. A. Isaacson, *Gravitational Radiation in the Limit of High Frequency. I. The Linear Approximation and Geometrical Optics*, *Physical Review* **166** (Feb., 1968) 1263–1271.

[20] R. A. Isaacson, *Gravitational Radiation in the Limit of High Frequency. II. Nonlinear Terms and the Effective Stress Tensor*, *Physical Review* **166** (Feb., 1968) 1272–1279.

[21] G. F. R. Ellis and W. Stoeger, *The 'fitting problem' in cosmology*, *Class. Quant. Grav.* **4** (1987) 1697–1729.

[22] T. Futamase, *An approximation scheme for constructing inhomogeneous universes in general relativity*, *MNRAS* **237** (Mar., 1989) 187–200.

[23] T. Buchert and J. Ehlers, *Averaging inhomogeneous Newtonian cosmologies*, *Astron.Astrophys.* **320** (1997) 1–7, [astro-ph/9510056].

[24] T. Buchert, *On average properties of inhomogeneous fluids in general relativity. 1. Dust cosmologies*, *Gen.Rel.Grav.* **32** (2000) 105–125, [gr-qc/9906015].

[25] A. Friedman, *Über die krümmung des raumes*, *Zeitschrift für Physik* **10** (1922), no. 1 377–386.

[26] G. Lemaître, *A homogeneous Universe of constant mass and growing radius accounting for the radial velocity of extragalactic nebulae*, *Annales Soc.Sci.Brux.Ser.I Sci.Math.Astron.Phys.* **A47** (1927) 49–59.

[27] H. P. Robertson, *Kinematics and World-Structure*, *Astrophys. J.* **82** (1935) 284–301.

[28] H. P. Robertson, *Kinematics and World-Structure. 2*, *Astrophys. J.* **83** (1935) 187–201.

[29] H. P. Robertson, *Kinematics and World-Structure. 3*, *Astrophys. J.* **83** (1936) 257–271.

[30] **Planck** Collaboration, P. A. R. Ade et al., *Planck 2015 results. XIII. Cosmological parameters*, arXiv:1502.01589.

[31] E. Poisson, *A Relativist's Toolkit*. Cambridge, 2004.

[32] A. Raychaudhuri, *Relativistic cosmology. 1.*, *Phys.Rev.* **98** (1955) 1123–1126.

[33] G. Ellis, *Relativistic cosmology*, *Gen.Rel.Grav.* **41** (2009) 581–660.

[34] G. F. R. Ellis and H. van Elst, *Cosmological models: Cargese lectures 1998*, *NATO Sci. Ser. C* **541** (1999) 1–116, [gr-qc/9812046].

[35] E. Curiel, *A Primer on Energy Conditions*, *ArXiv e-prints* (Apr., 2014) [arXiv:1405.0403].

[36] C. G. Tsagas, A. Challinor, and R. Maartens, *Relativistic cosmology and large-scale structure*, *Phys. Rept.* **465** (2008) 61–147, [arXiv:0705.4397].

[37] C.-H. Chuang, J.-A. Gu, and W.-Y. P. Hwang, *Inhomogeneity-induced cosmic acceleration in a dust universe*, *Class. Quant. Grav.* **25** (2008) 175001, [astro-ph/0512651].

[38] A. Paranjape and T. P. Singh, *The Possibility of Cosmic Acceleration via Spatial Averaging in Lemaitre-Tolman-Bondi Models*, *Class. Quant. Grav.* **23** (2006) 6955–6969, [astro-ph/0605195].

[39] S. Rasanen, *Applicability of the linearly perturbed FRW metric and Newtonian cosmology*, *Phys. Rev.* **D81** (2010) 103512, [arXiv:1002.4779].

[40] S. Rasanen, *Accelerated expansion from structure formation*, *JCAP* **0611** (2006) 003, [astro-ph/0607626].

[41] S. Rasanen, *Evaluating backreaction with the peak model of structure formation*, *JCAP* **0804** (2008) 026, [arXiv:0801.2692].

[42] P. Bull and T. Clifton, *Local and nonlocal measures of acceleration in cosmology*, *PRD* **85** (May, 2012) 103512, [arXiv:1203.4479].

[43] M. Mattsson and T. Mattsson, *On the role of shear in cosmological averaging*, *JCAP* **1010** (2010) 021, [arXiv:1007.2939].

[44] C. Clarkson and O. Umeh, *Is backreaction really small within concordance cosmology?*, *Classical and Quantum Gravity* **28** (Aug., 2011) 164010, [arXiv:1105.1886].

[45] T. Buchert, *Toward physical cosmology: focus on inhomogeneous geometry and its non-perturbative effects*, *Class. Quant. Grav.* **28** (2011) 164007, [arXiv:1103.2016].

[46] T. Buchert et al., *Is there proof that backreaction of inhomogeneities is irrelevant in cosmology?*, arXiv:1505.07800.

[47] A. Ishibashi and R. M. Wald, *Can the acceleration of our universe be explained by the effects of inhomogeneities?*, *Class. Quant. Grav.* **23** (2006) 235–250, [gr-qc/0509108].

[48] D. Baumann, A. Nicolis, L. Senatore, and M. Zaldarriaga, *Cosmological non-linearities as an effective fluid*, *JCAP* **7** (July, 2012) 51, [arXiv:1004.2488].

[49] S. R. Green and R. M. Wald, *A new framework for analyzing the effects of small scale inhomogeneities in cosmology*, *Phys. Rev.* **D83** (2011) 084020, [arXiv:1011.4920].

[50] S. R. Green and R. M. Wald, *Comments on Backreaction*, arXiv:1506.06452.

[51] J. Jackson, *Classical electrodynamics*. Wiley, 1975.

[52] E. F. P. Schneider, J. Ehlers, *Gravitational Lenses*. Springer, 1992.

[53] D. W. Hogg, *Distance measures in cosmology*, astro-ph/9905116.

[54] I. M. H. Etherington, *On the Definition of Distance in General Relativity.*, *Philosophical Magazine* **15** (1933) 761.

[55] I. M. H. Etherington, *Republication of: LX. On the definition of distance in general relativity*, *General Relativity and Gravitation* **39** (July, 2007) 1055–1067.

[56] R. Wald, *General Relativity*. The University of Chicago Press, 1984.

[57] S. Magni, *Backreaction and the Covariant Formalism of General Relativity*. PhD thesis, Pavia U., 2012. arXiv:1202.0430.

[58] B. Leibundgut, *Supernovae and Cosmology*, *Gen. Rel. Grav.* **40** (2008) 221, [arXiv:0802.4154].

[59] L. Ferrario, *Binary Paths to Type Ia Supernovae Explosions: the Highlights*, in *IAU Symposium* (R. Di Stefano, M. Orio, and M. Moe, eds.), vol. 281 of *IAU Symposium*, pp. 341–350, Jan., 2013. arXiv:1209.1201.

[60] **Supernova Search Team** Collaboration, J. L. Tonry et al., *Cosmological results from high-z supernovae*, *Astrophys. J.* **594** (2003) 1–24, [astro-ph/0305008].

[61] **Supernova Search Team** Collaboration, A. G. Riess et al., *Type Ia supernova discoveries at $z > 1$ from the Hubble Space Telescope: Evidence for past deceleration and constraints on dark energy evolution*, *Astrophys. J.* **607** (2004) 665–687, [astro-ph/0402512].

[62] **SNLS** Collaboration, P. Astier et al., *The Supernova legacy survey: Measurement of omega(m), omega(lambda) and W from the first year data set*, *Astron. Astrophys.* **447** (2006) 31–48, [astro-ph/0510447].

[63] **Supernova Cosmology Project** Collaboration, R. Amanullah et al., *Spectra and Light Curves of Six Type Ia Supernovae at $0.511 < z < 1.12$ and the Union2 Compilation*, *ApJ* **716** (2010) 712–738, [arXiv:1004.1711].

[64] **Supernova Cosmology Project** Collaboration, N. Suzuki et al., *The Hubble Space Telescope Cluster Supernova Survey. V. Improving the Dark-energy Constraints above $z > 1$ and Building an Early-type-hosted Supernova Sample*, *ApJ* **746** (Feb., 2012) 85, [arXiv:1105.3470].

[65] **SNLS** Collaboration, A. Conley et al., *Supernova Constraints and Systematic Uncertainties from the First 3 Years of the Supernova Legacy Survey*, *ApJS* **192** (2011) 1, [arXiv:1104.1443].

[66] **SDSS** Collaboration, M. Betoule et al., *Improved cosmological constraints from a joint analysis of the SDSS-II and SNLS supernova samples*, *Astron. Astrophys.* **568** (2014) A22, [arXiv:1401.4064].

[67] G. R. Bengochea, *Supernova light-curve fitters and dark energy*, *Physics Letters B* **696** (Jan., 2011) 5–12, [arXiv:1010.4014].

[68] C. Clarkson, B. Bassett, and T. H.-C. Lu, *A general test of the Copernican Principle*, *Phys.Rev.Lett.* **101** (2008) 011301, [arXiv:0712.3457].

[69] A. Shafieloo and C. Clarkson, *Model independent tests of the standard cosmological model*, *Phys. rev. D* **81** (Apr., 2010) 083537, [arXiv:0911.4858].

[70] E. Mortsell and J. Jonsson, *A model independent measure of the large scale curvature of the Universe*, *ArXiv e-prints* (Feb., 2011) [arXiv:1102.4485].

[71] W. Hu and S. Dodelson, *Cosmic microwave background anisotropies*, *Ann. Rev. Astron. Astrophys.* **40** (2002) 171–216, [astro-ph/0110414].

[72] S. Dodelson, *Modern Cosmology*. Academic Press, Amsterdam, 2003.

[73] R. Durrer, *The cosmic microwave backgrond*, *PoS* **CARGESE2007** (2007) 006.

[74] R. Durrer, *The cosmic microwave background: the history of its experimental investigation and its significance for cosmology*, *Class. Quant. Grav.* **32** (2015), no. 12 124007, [arXiv:1506.01907].

[75] R. Sachs and A. Wolfe, *Perturbations of a cosmological model and angular variations of the microwave background*, *ApJ* **147** (1967) 73–90.

[76] M. Rees and D. Sciama, *Large scale Density Inhomogeneities in the Universe*, *Nature* **217** (1968) 511–516.

[77] B. R. Granett, M. C. Neyrinck, and I. Szapudi, *An Imprint of Super-Structures on the Microwave Background due to the Integrated Sachs-Wolfe Effect*, *Astrophys.J.* **683** (2008) L99–L102, [arXiv:0805.3695].

[78] S. Hotchkiss, S. Nadathur, S. Gottlöber, I. T. Iliev, A. Knebe, W. A. Watson, and G. Yepes, *The Jubilee ISW Project – II. Observed and simulated imprints of voids and superclusters on the cosmic microwave background*, *Mon. Not. Roy. Astron. Soc.* **446** (2015) 1321–1334, [arXiv:1405.3552].

[79] **Planck** Collaboration, P. A. R. Ade et al., *Planck 2015 results. XVII. Constraints on primordial non-Gaussianity*, arXiv:1502.01592.

[80] H. K. Eriksen, F. K. Hansen, A. J. Banday, K. M. Gorski, and P. B. Lilje, *Asymmetries in the Cosmic Microwave Background anisotropy field*, *Astrophys. J.* **605** (2004) 14–20, [astro-ph/0307507]. [Erratum: Astrophys. J.609,1198(2004)].

[81] J. Hoftuft, H. K. Eriksen, A. J. Banday, K. M. Gorski, F. K. Hansen, and P. B. Lilje, *Increasing evidence for hemispherical power asymmetry in the five-year WMAP data*, *Astrophys. J.* **699** (2009) 985–989, [arXiv:0903.1229].

[82] **Planck** Collaboration, P. A. R. Ade, N. Aghanim, C. Armitage-Caplan, M. Arnaud, M. Ashdown, F. Atrio-Barandela, J. Aumont, C. Baccigalupi, A. J. Banday, and et al., *Planck 2013 results. XXIII. Isotropy and statistics of the CMB*, *ArXiv e-prints* (Mar., 2013) [arXiv:1303.5083].

[83] S. Flender and S. Hotchkiss, *The small scale power asymmetry in the cosmic microwave background*, *JCAP* **1309** (2013) 033, [arXiv:1307.6069].

[84] P. Vielva, *A Comprehensive Overview of the Cold Spot*, *Advances in Astronomy* **2010** (2010) [arXiv:1008.3051].

[85] O. Chwolson, *Über eine mögliche Form fiktiver Doppelsterne*, *Astronomische Nachrichten* **221** (June, 1924) 329.

[86] A. Einstein, *Lens-Like Action of a Star by the Deviation of Light in the Gravitational Field*, *Science* **84** (Dec., 1936) 506–507.

[87] R. D. Blandford, A. B. Saust, T. G. Brainerd, and J. V. Villumsen, *The distortion of distant galaxy images by large-scale structure*, *Mon. Not. Roy. Astron. Soc.* **251** (1991) 600–627.

[88] N. Kaiser, *Weak gravitational lensing of distant galaxies*, *ApJ* **388** (Apr., 1992) 272–286.

[89] N. Kaiser, G. Squires, and T. Broadhurst, *A Method for Weak Lensing Observations*, *ApJ* **449** (Aug., 1995) 460, [astro-ph/9411005].

[90] M. Bartelmann and P. Schneider, *Weak gravitational lensing*, *Phys.Rept.* **340** (2001) 291–472, [astro-ph/9912508].

[91] A. Lewis and A. Challinor, *Weak gravitational lensing of the CMB:*, *Phys. Rept.* **429** (2006) 1–65, [astro-ph/0601594].

[92] **Planck** Collaboration, P. Ade et al., *Planck 2015 results. XV. Gravitational lensing*, arXiv:1502.01591.

[93] T. Pyne and S. M. Carroll, *Higher order gravitational perturbations of the cosmic microwave background*, *Phys. Rev.* **D53** (1996) 2920–2929, [astro-ph/9510041].

[94] S. Mollerach and S. Matarrese, *Cosmic microwave background anisotropies from second order gravitational perturbations*, *Phys. Rev.* **D56** (1997) 4494–4502, [astro-ph/9702234].

[95] E. Bertschinger, *Cosmological dynamics: Course 1*, in *Summer School on Cosmology and Large Scale Structure (Session 60) Les Houches, France, August 1-28, 1993*, 1993. astro-ph/9503125.

[96] M. Bruni, S. Matarrese, S. Mollerach, and S. Sonego, *Perturbations of space-time: Gauge transformations and gauge invariance at second order and beyond*, *Class. Quant. Grav.* **14** (1997) 2585–2606, [gr-qc/9609040].

[97] K. Tomita, *Relativistic second-order perturbations of nonzero-Λ flat cosmological models and CMB anisotropies*, *Phys. rev. D* **71** (Apr., 2005) 083504, [astro-ph/0501663].

[98] K. Tomita, *Second-order gravitational effects of local inhomogeneities on CMB anisotropies in nonzero-Λ flat cosmological models*, *Phys. rev. D* **72** (Aug., 2005) 043526, [astro-ph/0505157].

[99] K. Tomita and K. T. Inoue, *Second order gravitational effects on CMB temperature anisotropy in Λ dominated flat universes*, *Phys. rev. D* **77** (May, 2008) 103522, [arXiv:0712.1291].

[100] S. Nadathur, S. Hotchkiss, and S. Sarkar, *The integrated Sachs-Wolfe imprints of cosmic superstructures: a problem for ΛCDM*, *JCAP* **1206** (2012) 042, [arXiv:1109.4126].

[101] G. Lemaître, *The expanding universe*, *Gen. Rel. Grav.* **29** (1997) 641–680. [Annales Soc. Sci. Brux. Ser. I Sci. Math. Astron. Phys.A53,51(1933)].

[102] R. C. Tolman, *Effect of imhomogeneity on cosmological models*, *Proc.Nat.Acad.Sci.* **20** (1934) 169–176.

[103] H. Bondi, *Spherically symmetrical models in general relativity*, *Mon.Not.Roy.Astron.Soc.* **107** (1947) 410–425.

[104] J. Plebanski and A. Krasinski, *An introduction to general relativity and cosmology*. Cambridge University Press, 2006.

[105] J. Silk, *Large-scale inhomogeneity of the Universe - Spherically symmetric models*, *A&A* **59** (July, 1977) 53–58.

[106] C. Hellaby and K. Lake, *Shell crossings and the Tolman model*, *Astrophys.J.* **290** (1985) 381.

[107] P. Szekeres and A. Lun, *What is a shell crossing singularity?*, *J. Austral. Math. Soc.* **B41** (1999) 167–179.

[108] P. S. Joshi and I. H. Dwivedi, *Naked singularities in spherically symmetric inhomogeneous Tolman-Bondi dust cloud collapse*, *Phys. Rev.* **D47** (1993) 5357–5369, [gr-qc/9303037].

[109] I. H. Dwivedi and P. S. Joshi, *On the occurrence of naked singularity in spherically symmetric gravitational collapse*, *Comm. Math. Phys.* **166** (1994), no. 1 117–128.

[110] P. Fleury, *Swiss-cheese models and the Dyer-Roeder approximation*, *JCAP* **1406** (2014) 054, [arXiv:1402.3123].

[111] N. Brouzakis, N. Tetradis, and E. Tzavara, *The Effect of Large-Scale Inhomogeneities on the Luminosity Distance*, *JCAP* **0702** (2007) 013, [astro-ph/0612179].

[112] P. Szekeres, *A Class of Inhomogeneous Cosmological Models*, *Commun.Math.Phys.* **41** (1975) 55.

[113] K. Bolejko, A. Krasinski, C. Hellaby, and M.-N. Celerier, *Structures in the Universe by exact methods: formation, evolution, interactions*, .

[114] C. Hellaby and A. Krasinski, *Physical and geometrical interpretation of the epsilon <= 0 Szekeres models*, *Phys. Rev.* **D77** (2008) 023529, [arXiv:0710.2171].

[115] A. Krasinski, *Geometry and topology of the quasi-plane Szekeres model*, *Phys. Rev.* **D78** (2008) 064038, [arXiv:0805.0529]. [Erratum: Phys. Rev.D85,069903(2012)].

[116] E. Di Dio, M. Vonlanthen, and R. Durrer, *Back reaction from walls*, *JCAP* **2** (Feb., 2012) 36, [arXiv:1111.5764].

[117] A. Einstein and E. G. Straus, *The influence of the expansion of space on the gravitation fields surrounding the individual stars*, *Rev.Mod.Phys.* **17** (1945) 120–124.

[118] G. Darmois, *Les équations de la gravitation einsteinienne*. Gauthier-Villars, 1927.

[119] W. Israel, *Singular hypersurfaces and thin shells in general relativity*, *Nuovo Cim.* **B44S10** (1966) 1.

[120] E. Martinez-Gonzalez, J. L. Sanz, and J. Silk, *Anisotropies in the microwave sky due to nonlinear structures*, *ApJ* **355** (May, 1990) L5–L9.

[121] E. Martinez-Gonzalez and J. L. Sanz, *CMB Anisotropies Generated by Cosmic Voids and Great Attractors*, *MNRAS* **247** (Dec., 1990) 473–478.

[122] M. Panek, *Cosmic background radiation anisotropies from cosmic structures - Models based on the Tolman solution*, *ApJ* **388** (Apr., 1992) 225–233.

[123] J. V. Arnau, M. J. Fullana, L. Monreal, and D. Saez, *On the microwave background anisotropies produced by nonlinear voids*, *ApJ* **402** (Jan., 1993) 359–368.

[124] M. J. Fullana, D. Saez, and J. V. Arnau, *On the microwave background anisotropy produced by Great Attractor-like structures*, *ApJS* **94** (Aug., 1994) 1–16.

[125] K. T. Inoue and J. Silk, *Local voids as the origin of large-angle cosmic microwave background anomalies I*, *Astrophys. J.* **648** (2006) 23–30, [astro-ph/0602478].

[126] K. T. Inoue and J. Silk, *Local Voids as the Origin of Large-angle Cosmic Microwave Background Anomalies: The Effect of a Cosmological Constant*, *Astrophys. J.* **664** (2007) 650–659, [astro-ph/0612347].

[127] N. Mustapha, C. Hellaby, and G. Ellis, *Large scale inhomogeneity versus source evolution: Can we distinguish them observationally?*, *Mon.Not.Roy.Astron.Soc.* **292** (1997) 817–830, [gr-qc/9808079].

[128] H. Alnes, M. Amarzguioui, and O. Gron, *An inhomogeneous alternative to dark energy?*, *Phys. Rev.* **D73** (2006) 083519, [astro-ph/0512006].

[129] K. Enqvist and T. Mattsson, *The effect of inhomogeneous expansion on the supernova observations*, *JCAP* **0702** (2007) 019, [astro-ph/0609120].

[130] S. Alexander, T. Biswas, A. Notari, and D. Vaid, *Local Void vs Dark Energy: Confrontation with WMAP and Type Ia Supernovae*, *JCAP* **0909** (2009) 025, [arXiv:0712.0370].

[131] J. Garcia-Bellido and T. Haugbølle, *Confronting Lemaitre Tolman Bondi models with observational cosmology*, *JCAP* **4** (Apr., 2008) 3, [arXiv:0802.1523].

[132] J. García-Bellido and T. Haugbølle, *Looking the void in the eyes — the kinematic Sunyaev Zeldovich effect in Lemaître Tolman Bondi models*, *JCAP* **9** (Sept., 2008) 16, [arXiv:0807.1326].

[133] J. García-Bellido and T. Haugbølle, *The radial BAO scale and cosmic shear, a new observable for inhomogeneous cosmologies*, *JCAP* **9** (Sept., 2009) 28, [arXiv:0810.4939].

[134] T. Biswas, A. Notari, and W. Valkenburg, *Testing the Void against Cosmological data: fitting CMB, BAO, SN and H0*, *JCAP* **1011** (2010) 030, [arXiv:1007.3065].

[135] A. Moss, J. P. Zibin, and D. Scott, *Precision Cosmology Defeats Void Models for Acceleration*, *Phys. Rev.* **D83** (2011) 103515, [arXiv:1007.3725].

[136] P. Sundell, E. Mörtsell, and I. Vilja, *Can a void mimic the Λ in ΛCDM?*, arXiv:1503.08045.

[137] L. Cayon, J. L. Sanz, E. Martinez-Gonzalez, A. J. Banday, F. Argueso, J. E. Gallegos, K. M. Gorski, and G. Hinshaw, *Spherical mexican hat wavelet: an application to detect non-gaussianity in the cobe-dmr maps*, *Mon. Not. Roy. Astron. Soc.* **326** (2001) 1243, [astro-ph/0105111].

[138] P. Vielva, E. Martinez-Gonzalez, R. B. Barreiro, J. L. Sanz, and L. Cayon, *Detection of non-Gaussianity in the WMAP 1 - year data using spherical wavelets*, *Astrophys. J.* **609** (2004) 22–34, [astro-ph/0310273].

[139] **Planck** Collaboration, P. A. R. Ade et al., *Planck 2015 results. XVI. Isotropy and statistics of the CMB*, arXiv:1506.07135.

[140] M. Cruz, E. Martínez-González, P. Vielva, J. M. Diego, M. Hobson, and N. Turok, *The CMB cold spot: texture, cluster or void?*, *MNRAS* **390** (Nov., 2008) 913–919, [arXiv:0804.2904].

[141] K. T. Inoue, *On the origin of the cold spot*, *MNRAS* **421** (Apr., 2012) 2731–2736, [arXiv:1109.4527].

[142] I. Szapudi, A. Kovács, B. R. Granett, Z. Frei, J. Silk, W. Burgett, S. Cole, P. W. Draper, D. J. Farrow, N. Kaiser, E. A. Magnier, N. Metcalfe, J. S. Morgan, P. Price, J. Tonry, and R. Wainscoat, *Detection of a Supervoid Aligned with the Cold Spot of the Cosmic Microwave Background*, *ArXiv e-prints* (May, 2014) [arXiv:1405.1566].

[143] F. Finelli, J. Garcia-Bellido, A. Kovacs, F. Paci, and I. Szapudi, *A Supervoid Imprinting the Cold Spot in the Cosmic Microwave Background*, *ArXiv e-prints* (May, 2014) [arXiv:1405.1555].

[144] **WMAP** Collaboration, C. L. Bennett, R. S. Hill, G. Hinshaw, D. Larson, K. M. Smith, J. Dunkley, B. Gold, M. Halpern, N. Jarosik, A. Kogut, E. Komatsu, M. Limon, S. S. Meyer, M. R. Nolta, N. Odegard, L. Page, D. N. Spergel, G. S. Tucker, J. L. Weiland, E. Wollack, and E. L. Wright, *Seven-year Wilkinson Microwave Anisotropy Probe (WMAP) Observations: Are There Cosmic Microwave Background Anomalies?*, *ApJS* **192** (Feb., 2011) 17, [arXiv:1001.4758].

[145] R. Kantowski, *Corrections in the Luminosity-Redshift Relations of the Homogeneous Fried-Mann Models*, *ApJ* **155** (Jan., 1969) 89.

[146] N. Sugiura, K.-i. Nakao, D. Ida, N. Sakai, and H. Ishihara, *How do nonlinear voids affect light propagation?*, *Prog.Theor.Phys.* **103** (2000) 73–89, [astro-ph/9912414].

[147] V. Marra, E. W. Kolb, S. Matarrese, and A. Riotto, *On cosmological observables in a swiss-cheese universe*, *Phys.Rev.* **D76** (2007) 123004, [arXiv:0708.3622].

[148] T. Biswas and A. Notari, *Swiss-Cheese Inhomogeneous Cosmology and the Dark Energy Problem*, *JCAP* **0806** (2008) 021, [astro-ph/0702555].

[149] K. Bolejko and M.-N. Celerier, *Szekeres Swiss-Cheese model and supernova observations*, *Phys.Rev.* **D82** (2010) 103510, [arXiv:1005.2584].

[150] S. J. Szybka, *On light propagation in Swiss-Cheese cosmologies*, *Phys.Rev.* **D84** (2011) 044011, [arXiv:1012.5239].

[151] C. Clarkson, G. F. Ellis, A. Faltenbacher, R. Maartens, O. Umeh, and J.-P. Uzan, *(Mis-)Interpreting supernovae observations in a lumpy universe*, *Mon.Not.Roy.Astron.Soc.* **426** (2012) 1121–1136, [arXiv:1109.2484].

[152] E. E. Flanagan, N. Kumar, and I. Wasserman, *Luminosity distance in Swiss cheese cosmology with randomized voids and galaxy halos*, *Phys.Rev.* **D88** (2013), no. 4 043004, [arXiv:1207.3711].

[153] K. Bolejko, C. Clarkson, R. Maartens, D. Bacon, N. Meures, and E. Beynon, *Antilensing: The Bright Side of Voids*, *Physical Review Letters* **110** (Jan., 2013) 021302, [arXiv:1209.3142].

[154] P. Fleury, H. Dupuy, and J.-P. Uzan, *Interpretation of the Hubble diagram in a nonhomogeneous universe*, *Phys.Rev.* **D87** (2013), no. 12 123526, [arXiv:1302.5308].

[155] P. Fleury, H. Dupuy, and J.-P. Uzan, *Can all cosmological observations be accurately interpreted with a unique geometry?*, *Phys.Rev.Lett.* **111** (2013) 091302, [arXiv:1304.7791].

[156] A. Peel, M. Troxel, and M. Ishak, *Effect of inhomogeneities on high precision measurements of cosmological distances*, arXiv:1408.4390.

[157] S. Weinberg, *Apparent luminosities in a locally inhomogeneous universe*, *ApJ* **208** (Aug., 1976) L1–L3.

[158] T. Kibble and R. Lieu, *Average magnification effect of clumping of matter*, *Astrophys.J.* **632** (2005) 718–726, [astro-ph/0412275].

[159] G. Ellis, B. Bassett, and P. Dunsby, *Lensing and caustic effects on cosmological distances*, *Class.Quant.Grav.* **15** (1998) 2345–2361, [gr-qc/9801092].

[160] N. Kaiser and J. A. Peacock, *On the Bias of the Distance-Redshift Relation from Gravitational Lensing*, arXiv:1503.08506.

[161] R. A. Vanderveld, E. E. Flanagan, and I. Wasserman, *Luminosity distance in 'Swiss cheese' cosmology with randomized voids: I. Single void size*, *Phys. Rev.* **D78** (2008) 083511, [arXiv:0808.1080].

[162] C. C. Dyer and R. C. Roeder, *The Distance-Redshift Relation for Universes with no Intergalactic Medium*, *ApJ* **174** (1972) L115.

[163] C. Dyer and R. Roeder, *Distance-Redshift Relations for Universes with Some Intergalactic Medium*, *Astrophys.J.* **180** (1973) L31.

[164] C. C. Dyer and R. C. Roeder, *Observations in Locally Inhomogeneous Cosmological Models*, *ApJ* **189** (1974) 167–176.

[165] C. Bonvin, R. Durrer, and M. A. Gasparini, *Fluctuations of the luminosity distance*, *Phys.Rev.* **D73** (2006) 023523, [astro-ph/0511183].

[166] C. Bonvin, *Effect of Peculiar Motion in Weak Lensing*, *Phys. Rev.* **D78** (2008) 123530, [arXiv:0810.0180].

[167] F. Bernardeau, C. Bonvin, and F. Vernizzi, *Full-sky lensing shear at second order*, *Phys. rev. D* **81** (Apr., 2010) 083002, [arXiv:0911.2244].

[168] C. Clarkson, *The general theory of secondary weak gravitational lensing*, arXiv:1503.08660.

[169] C. Clarkson, O. Umeh, R. Maartens, and R. Durrer, *What is the distance to the CMB?*, arXiv:1405.7860.

[170] C. Bonvin, C. Clarkson, R. Durrer, R. Maartens, and O. Umeh, *Do we care about the distance to the CMB? Clarifying the impact of second-order lensing*, arXiv:1503.07831.

[171] C. Bonvin, C. Clarkson, R. Durrer, R. Maartens, and O. Umeh, *Cosmological ensemble and directional averages of observables*, arXiv:1504.01676.

[172] K. Gorski, E. Hivon, A. Banday, B. Wandelt, F. Hansen, M. Reinecke, and M. Bartelman, *HEALPix - A Framework for high resolution discretization, and fast analysis of data distributed on the sphere*, *Astrophys.J.* **622** (2005) 759–771, [astro-ph/0409513].

[173] W. Valkenburg, *Swiss Cheese and a Cheesy CMB*, *JCAP* **0906** (2009) 010, [arXiv:0902.4698].